The dynamic crosstalk between cytoskeletal filaments regulates the cytoplasmic mechanics across the apicobasal axis

Dipanjan Ray[1], Deepak Kumar Sinha[1, *]

[1]School of Biological Sciences, Indian Association for the Cultivation of Science, Kolkata-700032, India

*Correspondence:

Deepak Kumar Sinha (bcdks@iacs.res.in)

School of Biological Sciences

Indian Association for the Cultivation of Science

Kolkata, 700032, India

Key words: Cytoplasmic mechanics, particle tracking microrheology, fractal dimension, vimentin, plectin, NF-κB

Abstract

The cytoplasm exhibits viscoelastic properties, displaying both solid and liquid-like behavior, and can actively regulate its mechanical attributes. The cytoskeleton is a major regulator among the numerous factors influencing cytoplasmic mechanics. We explore the interdependence of various cytoskeletal filaments and the impact of their density on cytoplasmic viscoelasticity. The heterogeneous distribution of these filaments give rise to polarised mechanical properties of the cytoplasm along the apicobasal axis. Actin filament (F-actin) disassembly softens the basal cytoplasm

while stiffening the mid-cytoplasm due to increased vimentin filament assembly. Disruption of microtubules (MT) or depletion of vimentin softens both the basal and mid-cytoplasm. Cyto D treatment results in localised increase of vimentin assembly in the mid cytoplasm which is dependent on the cytolinker plectin. Nocodazole treatment has a negligible effect on F-actin distribution but significantly alters vimentin's spatial arrangement. We demonstrate that Cyto D treatment upregulates vimentin expression via ROS-mediated activation of NF-κB. This manuscript investigates how different cytoskeletal filaments influence the rheological characteristics of various cytoplasmic regions.

Introduction

The cytoplasm is a gel-like substance enclosed within the cell membrane that plays a critical role in maintaining cellular structure and facilitating various biochemical processes (Fels et al., 2009; Pollard, 1976; Trevors, 2011). It exhibits viscoelastic properties, possessing both viscous and elastic characteristics that enable it to function effectively (Moeendarbary et al., 2013). This unique nature allows the cytoplasm to behave like a fluid under slow deformations, permitting the smooth movement and distribution of organelles and molecules (Hu et al., 2017). Conversely, it acts like an elastic solid when subjected to rapid stress (Munder et al., 2016). This viscoelasticity is crucial for cellular processes such as motility (Bray, 2000), cell division (Xie et al., 2022), and intracellular transport (Guigas et al., 2007), providing the necessary resilience and flexibility. The viscoelastic properties of the cytosol are influenced by several factors, including the composition and organization of the cytoskeleton (Bausch et al., 1998), the concentration of cytoplasmic proteins (Ellis, 2001; Zimmerman & Minton, 1993), and the presence of cellular organelles (Najafi et al., 2023). The cytoskeleton, consisting of actin, microtubules, and intermediate

filaments, provides structural support that enhances the cytoplasm's elasticity and its capacity to withstand mechanical stress (Pegoraro et al., 2017). The density and cross-linking of these filaments directly affect the cytoplasm's mechanical properties (Pegoraro et al., 2017). The density and distribution of cytoskeletal filaments are heterogeneous across the cytoplasm. For example, actin filaments typically form a dense meshwork at the cell periphery, offering structural support and aiding in cell shape maintenance (Svitkina, 2020). In contrast, in the cell interior, actin filaments may organize into stress fibers, facilitating cell contraction and motility (Tojkander et al., 2012). Similarly, microtubule filaments exhibit a dynamic distribution pattern throughout the cytoplasm, extending from the microtubule organizing centre (MTOC) towards the cell periphery (Sanchez & Feldman, 2017; Schuh & Ellenberg, 2007). Vimentin, a type III intermediate filament protein, is essential for maintaining cellular integrity, providing mechanical strength, and supporting cellular structures (Liu et al., 2015). Vimentin filaments form a network that resists mechanical stress (Mendez et al., 2014). These filaments create a dynamic network within the cytoplasm, enveloping the nucleus and extending throughout the cell to provide structural support and organization (Zhang et al., 2021). Studies have shown that de novo assembly of vimentin filaments throughout the cytoplasm significantly contributes to the cytoskeletal architecture (Sarria et al., 1990). These cytoskeletal components can interact either directly or via cytoskeletal cross-linkers such as plectin (Wiche, 1998). The interactions between these filaments create a dynamic, meshwork-like pattern within the cytoplasm, which can reorganise in response to various internal and external stimuli (Hohmann & Dehghani, 2019). The distribution of these cytoskeletal filaments varies across different regions of a cell, leading to significant heterogeneity in the cytoplasmic mechanical properties. Several studies have been conducted on the

mechanical properties of the cytoplasm, but most provide information about the overall mechanical behaviour without offering much detail about the localised viscoelastic properties of different cytoplasmic regions. The rheology of cytoskeletal filaments has been extensively characterised in various in vitro setups; however, their behaviour inside the cytoplasm is not well understood and may differ significantly. Additionally, how the density and crosstalk between the cytoskeletal filaments affect cytoplasmic mechanics across the apicobasal axis remains elusive. This study reports that the density of actin, microtubule, and vimentin filaments is anisotropic along the apicobasal axis of NIH 3T3 fibroblasts. Using particle tracking microrheology (PTM), we demonstrate that the mechanical properties of the cytoplasm along the apicobasal axis are directly influenced by the density of these cytoskeletal filaments. This manuscript establishes the role of individual cytoskeletal filaments in determining the local mechanical properties of the basal and mid-cytoplasm. Furthermore, our findings indicate that crosstalk between cytoskeletal components is crucial for maintaining the mechanical integrity of the cytoplasm. Additionally, we report that the actin-disrupting agent Cyto D enhances the expression of vimentin via ROS-dependent activation of NF-κB.

Results

Mechanical properties of the cytoplasm are polarised along the apicobasal axis

The cytoplasm contains various cytoskeletal components, such as actin microfilaments, microtubules (MT) and intermediate filaments (IF) (Hohmann & Dehghani, 2019). However, their distribution and abundance are not uniform and vary along the apicobasal axis. **Figure 1A** illustrates the distribution of these three major cytoskeletal filaments: actin, microtubules, and vimentin (a type III intermediate filament). This heterogeneous distribution results in locally variable mechanical properties of the cytosol (Fletcher & Mullins, 2010). To evaluate these local mechanical properties, we analysed the trajectories (r(t)) of fluorescently labelled microspheres, each with a diameter of 200 nm, scattered throughout the cytoplasm (**Figure 1B**). The trajectories were derived by monitoring the random, spontaneous movement of the microsphere centroids across 1000 frames over a 20-second duration, corresponding to one frame every 20 milliseconds. These microspheres serve as probes for the local viscoelastic properties of the cytoplasm. The mean squared displacement (MSD) values obtained from the trajectories of these microspheres provide insight into the local viscoelastic properties of the cytoplasm. The time-scale-dependent compliance values derived from MSDs describe the local deformability of the cytoplasm in response to thermal forces ~ kBT/a. Here, kB, T, and a represent Boltzmann's constant, the absolute temperature of the medium, and the radius of the microsphere, respectively. These forces arise from the thermal fluctuations of the probe microspheres (Wirtz, 2009). **Figure 1C** compares MSDs and compliance of the most and least compliant cytoplasmic regions at ten different locations within a given cell. Consistent with previous findings (Tseng et al., 2002), our results suggest that local deformability varies significantly throughout the cytoplasm of a cell. It is presumed that

116 the average density of cytoskeletal filaments varies along the apicobasal axis of the
117 cytoplasm (**Figure 1A**). Therefore, we hypothesised that these variations in
118 cytoskeletal filaments contributed to the polarisation of the locally heterogeneous
119 mechanical properties of the cytoplasm along the apicobasal axis. To resolve the
120 mechanical properties along the apicobasal axis, regions within $0 < z < 2$ microns and
121 $z > 2$ microns are designated as the basal and mid / apical regions of the cytoplasm,
122 respectively (**Figure 1A**). We designated the first sharply focused DIC image of the
123 edge of the cell as the basal plane during particle tracking microrheology (PTM), while
124 when calculating the fractal dimension (FD) values, the basal plane was determined
125 based on the presence of well-focused actin stress fibres (Maninová & Vomastek,
126 2016). To minimise the ambiguity that arises from height variations between different
127 cells, we selected cells that had comparable heights (~4±1μm). A histogram of the cell
128 heights used for analysis is presented in **Figure S1-A**. By analysing the trajectories
129 of at least 60 microspheres embedded in the basal or mid-cytoplasmic regions of at
130 least 10 different cells (**Figure S1-B** and **S1-C**), we determined the mechanical
131 properties of the cytoplasm along the apicobasal axis. **Figure 1D** compares the
132 average MSDs and compliance values of microspheres distributed in the mid and
133 basal cytoplasmic regions of at least 10 different cells. The mean MSDs indicated that
134 the mid cytoplasm demonstrated higher compliance compared to the basal cytoplasm.
135 The frequency-dependent viscoelastic moduli are algebraically derived from these
136 MSD values (Mason, 2000). The dynamic viscosity, η, is calculated by dividing the
137 viscous modulus, G'', by the corresponding angular frequency, ω. Given the frequency
138 dependence of mechanical properties, we analysed the elastic modulus (G') and
139 dynamic viscosity (η) at 1 Hz and 10 Hz frequencies to ensure uniformity in
140 comparisons across varying conditions. The elastic modulus (G') of the mid

141 cytoplasmic region was found to be significantly lower than that of the basal plane at
142 1Hz and 10Hz, indicating a softer cytoplasm at least 4-5 times (**Figure 1F-i, ii**). The
143 dynamic viscosity (η) of the mid cytoplasmic region remained at least 3 times lower
144 than the basal cytoplasmic region at both frequencies (**Figure 1F-iii, iv**). In
145 conclusion, the mechanical properties of the cytoplasm exhibited polarity along the
146 apicobasal axis, leading to a decrease in both stiffness and viscosity with increasing
147 cell height. When an elastic material undergoes deformation, it stores energy that can
148 be recovered upon stress release. However, in viscoelastic materials like cytoplasm,
149 some of this energy is also dissipated due to microstructural rearrangement, which
150 manifests as the viscous flow of the material. This dissipation of energy is indicated by
151 the dimensionless quantity known as the loss tangent, tan δ, which is the ratio between
152 viscous (G'') and elastic modulus (G'). A higher value of tan δ indicates that a greater
153 proportion of energy associated with deformation is dissipated as heat. The tan δ also
154 delineates viscoelastic solids from liquids. At the crossover frequency (ω_c), where the
155 elastic modulus (G'(ω)) intersects with the viscous modulus (G″(ω)), the mechanical
156 properties of the material undergo a transition from a viscoelastic solid (tan δ < 1) to a
157 viscoelastic liquid (tan δ > 1). The reciprocal of ω_c, designated as the relaxation time
158 (Schwarzl, 1971), represents the timescale over which the stored elastic stresses
159 dissipate due to spontaneous microstructural rearrangements. Given that the loss
160 tangent (tan δ) of the basal and mid cytoplasm remained above 1 across the frequency
161 spectrum of 1-10Hz (**Figure 1E**), it can be inferred that the cytoplasm exhibits
162 mechanical characteristics of a viscoelastic liquid. Furthermore, the decay of tan δ with
163 frequency and an apparent plateau near 10 Hz indicate that the relaxation time for
164 microstructural rearrangements of the cytoplasm is slower than 0.1 sec for both the
165 basal and mid regions of the cytoplasm. Next, we examined the relative density of

166 actin (**Figure 1G-i**), microtubule (**Figure 1G-ii**), and vimentin (**Figure 1G-iii**) filaments
167 across the basal ($0 < z < 2\mu m$), mid ($2\mu m < z < 4\mu m$) and apical ($z > 4\mu m$) cytoplasmic
168 regions. To quantify the density of cytoskeletal filaments, we computed their fractal
169 dimension (FD) values. The representative binary images of actin, vimentin, and
170 microtubule filaments across the apicobasal axis used for the FD analysis are
171 presented in **Figure S1-D**. **Figure 1H** compares the FD values of different cytoskeletal
172 filaments across the apicobasal axis. The relative abundance of these filaments varies
173 significantly in the basal cytoplasm; however, in the mid and apical regions, the
174 differences in their densities are negligible. Actin and vimentin filaments were
175 predominantly concentrated in the basal cytoplasm, with their densities gradually
176 decreasing towards the mid and apical regions. In contrast, microtubule (MT) filaments
177 showed relatively higher concentration around the mid cytoplasmic region compared
178 to the basal and apical regions. Based on **Figure 1H**, we deduced that disrupting actin
179 filaments would lead to distinct changes in the mechanical properties of the basal and
180 mid cytoplasm. Specifically, we anticipated that both regions would become softer due
181 to actin disassembly.

182 ***Disruption of actin filaments has contrasting effects on the mechanical***
183 ***properties of the basal and mid cytoplasm.***

184 Next, using cytochalasin D (Cyto D), we investigated the impact of actin filament
185 disruption on the mechanical properties of the basal and mid cytoplasmic regions. Cyto
186 D inhibits the polymerization of actin by binding to its barbed ends (Brown & Spudich,
187 1981; Casella et al., 1981; Cooper, 1987; Masiello et al., 1982). **Figure 2A** compares
188 the mechanical compliance, $\Gamma(t)$ and the MSD, between control and Cyto D treated
189 cells. Disruption of actin filaments by Cyto D reversed the mechanical polarity of the
190 cytoplasm along the apicobasal axis by making the mid cytoplasm less compliant than

the basal cytoplasm (**Figure 2A-i**). Comparison with control cells reveals that Cyto D treatment increased the compliance of the basal cytoplasm significantly (**Figure 2A-ii**), while the mid cytoplasm became slightly stiffer (**Figure 2A-iii**). Considering that the basal cytoplasm contained a higher concentration of actin filaments compared to the mid cytoplasm, we anticipated a significantly larger increase in the compliance of the basal plane than the mid cytoplasm due to actin disassembly. However, contrary to the anticipation we observed that actin disassembly caused a relatively smaller decrease of compliance in the mid cytoplasmic region (**Figure 2A-iii**). As anticipated, the disassembly of actin led to greater fluidization of the basal cytoplasm compared to the mid cytoplasm (**Figure S2-A**). Next, we examined the effect of actin disassembly on the elastic modulus (G’) and dynamic viscosity (η) of the basal and mid cytoplasm. A study by Rotsch & Radmacher (2000) reported that disassembly of actin filaments led to a significant decrease in the cell's elastic modulus, highlighting the critical role of the actin network in maintaining cellular mechanical stability. Similar to it, we found that the median elastic modulus (G') of the basal cytoplasm decreased significantly, by 8-10 fold at both 1 Hz and 10 Hz frequencies, due to the disassembly of actin filaments by cytochalasin D (**Figure 2B-i,ii**). Similarly, the dynamic viscosity (η) of the basal cytoplasm decreased 7-9 fold as a result of Cyto D treatment (**Figure 2B-iii,iv**). However, the effect of actin disruption on the mechanical properties (G' and η) of the mid cytoplasm is contrary to expectations (**Figure 2C**). Cyto D treatment caused a significant increase in both the elastic modulus (G') (**Figure 2C-i,ii**) and the dynamic viscosity (η) (**Figure 2C-iii,iv**) in the mid cytoplasm. To understand the reason behind the stiffening of the mid cytoplasm, we compared the density of actin filaments between control and Cyto D treated cells. Cyto D treatment (2 μM, 1 hour) resulted in the fragmentation of longer actin filaments into smaller segments (**Figure 2E-i**). Cyto

216 D mediated disassembly of actin caused significant loss of actin filaments in the basal,
217 mid and apical cytoplasm (**Figure 2D-i**). Therefore, we hypothesised that the observed
218 elevation in stiffness, as depicted in **Figure 2C**, despite the loss of actin filaments, was
219 due to the increased assembly of other cytoskeletal filaments within the mid
220 cytoplasmic region. The frequency dependence of the mid cytoplasm's loss tangent
221 further indicates that there are additional changes in the microstructure of the
222 cytoplasm other than the loss of actin filaments (**Figure S2-A** and **S2-C**). Next, we
223 explored the impact of actin disassembly on the density of microtubule and vimentin
224 filaments. Unlike actin filaments, Cyto D treatment did not have a significant effect on
225 the density of MT filaments (**Figure 2E-ii**). Analysis of FD values indicate that there
226 was no significant change in the density of MT filaments across the apicobasal axis
227 due to Cyto D treatment (**Figure 2D-ii**). Hence, MT filaments cannot be attributed to
228 the stiffening of the mid cytoplasm following Cyto D-induced disruption of actin
229 filaments. **Figure 1H** shows that the density of vimentin filaments was highest at the
230 basal cytoplasm and decreased gradually at the mid and apical cytoplasmic regions.
231 Treatment with Cyto D altered the distribution of vimentin filaments across the
232 apicobasal axis **(Figure 2D-iii)**. While the density of vimentin filaments showed no
233 significant changes in the basal and apical cytoplasm, the mid cytoplasm exhibited a
234 significant increase in the density of vimentin filaments in response to Cyto D
235 treatment. Confocal images clearly show the increased assembly of vimentin filaments
236 in the mid cytoplasm (**Figure 2E-iii**) of Cyto D treated cells. These observations
237 aligned with the observed increase in the elastic modulus (G') values of the mid
238 cytoplasm of Cyto D treated cells (**Figure 2C-i, ii**). Hence, we hypothesised that the
239 elevated assembly of vimentin filaments was responsible for the increased stiffness of
240 the mid cytoplasm in Cyto D treated cells.

Nocodazole-induced depolymerization of microtubules results in significant softening of the cytoplasm across the apicobasal axis.

Microtubules, like actin filaments, form intricate networks within the cytoplasm; however, their spatial arrangement significantly differs from that of actin filaments along the apicobasal axis (**Figure 1G-ii**, **Figure 1H**). Consequently, microtubule disassembly is expected to affect the mechanical properties of the cytoplasm differently from the disruption of actin filaments. We investigated the impact of microtubule disassembly on the mechanical properties of the basal and mid cytoplasmic regions. We used nocodazole to disrupt microtubules, which acts by interfering with their polymerisation (Xu et al., 2002). The effect of microtubule disassembly on the compliance of these cytoplasmic regions differed notably from that of actin filament perturbation. Unlike Cyto D treatment, the nocodazole treated cells retained the viscoelastic polarity along the apicobasal axis. The mid cytoplasm of nocodazole treated cells exhibited higher compliance compared to the basal cytoplasm (**Figure 3A-i**). A comparison between **Figure 3A-i** and **Figure 1D** demonstrated that the difference in compliance along the apicobasal axis increased by approximately 7-fold at 1 Hz and 9-fold at 10 Hz due to microtubule disassembly (**Figure S3-A**). The disassembly of microtubules led to a significant increase in compliance in both the basal (**Figure 3A-ii**) and mid cytoplasmic (**Figure 3A-iii**) regions compared to their counterparts in control cells. According to our observations, microtubule disruption had a pronounced effect on the compliance of the mid-cytoplasm compared to the basal cytoplasm. A 4 to 7 fold greater increase in compliance in the mid cytoplasm (**Figure S3-B**) further validated the higher density of microtubules within the mid cytoplasmic region compared to the basal region, as shown in **Figure 1H**. Interestingly the disassembly of microtubule makes the viscosity

266 and G' of the cytoplasm more polarised along the apicobasal axis (**Figure S3-E**). In
267 the mid cytoplasm, the disassembly of microtubules caused an intriguing change in its
268 mechanical properties. The mid-cytoplasm became more fluid-like at 10 Hz, while it
269 exhibited more gel-like characteristics at lower frequencies (**Figure S3-C**). The
270 frequency dependence of the mid-cytoplasm's loss tangent further indicated that there
271 were additional changes in the cytoplasm's microstructure other than the loss of
272 microtubule (**Figure S3-D**). Next, we probed the effect of Nocodazole treatment on
273 the other cytoskeletal filaments. Nocodazole treatment had an insignificant effect on
274 the FD of the actin filaments (**Figure 3D-i**, **Figure 3E-i**). As expected nocodazole
275 treatment (10uM, 1hr) severely altered the MT organization throughout the apicobasal
276 axis by reducing the density of the MT filaments (**Figure 3D-ii**, **Figure 3E-ii**). The
277 global loss of MT filaments upon nocodazole treatment justified the reduction in
278 cytoplasmic stiffness along the entire apicobasal axis. The MT disassembly had a
279 pronounced impact on the vimentin filament network (**Figure 3D-iii, Figure 3E-iii**). We
280 observed a significant reduction of vimentin filaments across the entire cytoplasm
281 (**Figure 3D-iii**). Most of the vimentin filaments were aggregated as thick strands
282 localised in the perinuclear region (**Figure 3E-iii**). Nocodazole treatment altered the
283 relative spatial distribution of vimentin filaments within the cell cytoplasm. In control
284 cells, we observed a decreasing vimentin filament density along the apicobasal axis
285 (**Figure 1H**). Conversely, in nocodazole-treated cells, the vimentin filament density
286 increased along the apicobasal axis (**Figure 3D-iii**). It is difficult to separate the
287 contribution of individual cytoskeletal filaments in governing the mechanical behaviour
288 of the cytoplasm. The basal cytoplasm of the nocodazole treated cells provides ideal
289 system to explore the mechanical characteristics of actin filaments in cells. The global

290 loss of vimentin filaments upon MT disassembly further contributed to the softening of
291 the basal and mid cytoplasmic regions.

292 ***Localised vimentin assembly stiffens mid cytoplasm in cytochalasin D treated***
293 ***cells***

294 The disruption of F-actin resulted in the rise of cytoplasmic stiffness in the mid
295 cytoplasmic region, with a concurrent increase in the density of vimentin filaments
296 (**Figure 2A-i** and **Figure 2D-ii**). Therefore, we hypothesised that the elevated levels
297 of vimentin filaments were responsible for the stiffening of the mid cytoplasm. To test
298 this hypothesis, we knocked out vimentin using CRISPR-Cas9 and investigated the
299 effect of Cyto D treatment on the mechanical properties of the mid cytoplasm in
300 vimentin knockout ($Vim^{-/-}$) cells. **Figure S4-A** validates the knockdown of vimentin.
301 The $Vim^{-/-}$ cells maintained the viscoelastic polarity of the cytoplasm along the
302 apicobasal axis (**Figure 4A-i**). A comparison of **Figure 4A-i** and **Figure 1D**
303 demonstrates that the polarity of compliance along the apicobasal axis slightly
304 decreased at 1 Hz and increased at 10 Hz due to the reduction of vimentin filaments
305 (**Figure S4-B**). The knockout of vimentin filaments made the basal and mid cytoplasm
306 more compliant than the control cells (**Figure 4A-ii, iii**). Further, we observed a larger
307 softening of the basal cytoplasm (75%) than the mid-cytoplasm (52%) at 1Hz due to
308 vimentin knockout (**Figure S4-C**). However, at 10Hz, mid-cytoplasm had a larger
309 softening than the basal cytoplasm (**Figure S4-C**). Cyto D treatment of $Vim^{-/-}$ cells
310 increased the compliance of the basal cytoplasm by an additional 5-fold at 1 Hz and
311 4-fold at 10 Hz (**Figure S4-D**). In contrast to the behaviour observed in wild-type cells,
312 $Vim^{-/-}$ cells did not exhibit reduced compliance or increased stiffness in the mid-
313 cytoplasm when subjected to Cyto D treatment. This established the role of vimentin
314 in the stiffening of the mid-cytoplasm upon Cyto D treatment as depicted in **Figure 2C**.

315 As anticipated, vimentin knockout caused a larger G' reduction in the basal (55%)
316 cytoplasm than in the mid (11%) cytoplasm (**Figure 4B**, **Figure 4C** and **Figure S4-E**).
317 The knockout of vimentin increased the polarity of G' and η along the apicobasal axis
318 (**Figure S4-F**). Additionally, vimentin depletion increased the fluidity of the mid-
319 cytoplasm at 1Hz (**Figure S4-G**). At 1 Hz, Cyto D treatment to Vim$^{-/-}$ cells reduced the
320 loss tangent (tan δ) of both the basal and mid cytoplasm. However, at 10 Hz, Cyto D
321 treatment increased the tan δ of the basal cytoplasm and had a negligible impact on
322 the tan δ of the mid cytoplasm. (**Figure S4-H**). Next, we investigated whether the
323 knockout of vimentin affected the spatial arrangement of actin and microtubule
324 filaments. The depletion of vimentin had an insignificant effect on the fractal dimension
325 (FD) of the actin filament and microtubule networks (**Figure 4D**). **Figure 4E** compares
326 the immunofluorescence images of the F-actin and microtubules at the basal, mid, and
327 apical cytoplasm in wild-type (WT) cells with Vim$^{-/-}$ cells. We observed no noticeable
328 changes in the spatial organisation of actin and microtubule filaments due to vimentin
329 knockout. The FD analysis (**Figure 4D**) supported this observation, suggesting that
330 the knockout of vimentin had an insignificant effect on actin and microtubule filament
331 networks in both the basal and mid-cytoplasm. Therefore, the altered mechanical
332 properties of Vim$^{-/-}$ cells can be attributed to the lack of vimentin filaments.

333 ***Plectin directs the localised assembly of vimentin filaments in the mid-***
334 ***cytoplasm of cytochalasin D treated cells***

335 The localised increase of vimentin filaments in Cyto D treated cells (**Figure 2D-iii** and
336 **2E-iii**) suggested that the formation of new filaments is controlled spatially within the
337 cytoplasm. To gain mechanistic insight into the localised growth of vimentin filaments
338 in the mid-cytoplasm, we investigated whether the existing vimentin molecules within
339 the filaments spatially reorganize or if the overexpression of vimentin in Cyto D-treated

340 cells forms new filaments localised in the mid-cytoplasm. While the levels of actin
341 (**Figure 5A**) and tubulin (**Figure 5B**) proteins were unaffected by Cyto D treatment,
342 the expression levels of vimentin showed a significant increase (**Figure 5C**).
343 Additionally, we observed a significant increase in the levels of vimentin mRNA due to
344 Cyto D treatment (**Figure 5D**). This indicates that the disassembly of actin by Cyto D
345 triggered the synthesis of additional vimentin proteins. Further, the newly formed
346 vimentin molecules preferentially assembled into filaments in the mid cytoplasm. We
347 speculated that crosslinkers such as plectin, which enable mechanosensitive
348 crosslinking of vimentin with F-actin (Marks et al., 2022) and microtubules (Svitkina et
349 al., 1996) in cells may control the localised growth of new vimentin filaments. To
350 validate our assumption, we depleted plectin using plectin siRNA (**Figure 5E**) and
351 investigated the effect of Cyto D treatment on the assembly of vimentin filaments in
352 transiently plectin-depleted cells. Treatment of Cyto D increased the levels of vimentin
353 protein (**Figure 5F**) and the mRNA (**Figure 5G**) in plectin-depleted cells. Unlike control
354 cells, the treatment of Cyto D led to an increase of vimentin density in both the basal
355 and mid cytoplasmic regions of plectin deficient cells (**Figure 5I and S5-D**). This
356 established the role of plectin in facilitating the localised assembly of vimentin in the
357 mid-cytoplasm after Cyto D treatment. Interestingly, we observed an increase in the
358 density of actin filaments in the form of stress fibers in the basal cytoplasm of plectin-
359 deficient cells (**Figure 5H and S5-D**). However, there was no observable change in
360 the total protein level of actin in plectin-depleted cells (**Figure S5-A**). This suggests
361 that the increase in actin filaments in the basal cytoplasm of plectin-depleted cells was
362 orchestrated by the spatial reorganisation of filamentous actin rather than an overall
363 increase in the level of total actin. Hence, we conclude that plectin helps maintain the
364 relative abundance of actin filaments and is essential for the localised increase in the

365 density of vimentin filaments in the mid-cytoplasmic region of Cyto D-treated cells. The
366 reorganisation of actin and vimentin filaments in plectin-depleted cells resulted in a
367 more gel-like consistency of the basal and mid cytoplasm at higher frequencies
368 (**Figure S5-B** and **S5-C**).

369 ***Cyto D induced assembly of vimentin is dependent on ROS-mediated activation***
370 ***of NF-κB pathway***

371 We observed that the disassembly of actin filaments by Cyto D caused an
372 overexpression of vimentin via transcriptional upregulation (**Figure 5D**). The newly
373 synthesized vimentin then assembled into filaments in the mid-cytoplasm (**Figure 2D-**
374 **iii**). The treatment of Cyto D produces ROS (Kustermans et al., 2005), which is known
375 to activate the transcription factor NF-κB (Morgan & Liu, 2011). Vimentin is a well
376 reported target of NF-κB (Marsigliante et al., 2016; Zhou et al., 2019). Therefore, we
377 speculated that Cyto D treatment activated NF-κB in NIH 3T3 cells through the
378 generation of ROS, subsequently triggering the transcription of vimentin. Additionally,
379 it remained unclear whether the elevation of ROS alone was sufficient or if the
380 disassembly of actin filaments was also required to trigger the transcription and
381 assembly of vimentin. Using the transient expression of EGFP-p65 in NIH 3T3 cells,
382 we established that Cyto D treatment activated NF-κB within 15 minutes (**Figure 6A-i**
383 and **6B-i**). We used an analogue of resveratrol, widely used as an NF-κB inhibitor, to
384 establish that Cyto D activated NF-κB via the canonical pathway (**Figure 6A-ii**).
385 Comparing the nuclear fraction of p65 in control cells with Cyto D-treated cells (**Figure**
386 **6C**) established that the Cyto D treatment activated the nuclear translocation of
387 endogenous p65. Further, in the presence of the NF-κB inhibitor, Cyto D treatment
388 failed to activate the transcription of vimentin (**Figure 6D-i**). This established that Cyto
389 D activated the transcription of vimentin through NF-κB. The negligible change in the

density of vimentin along the apicobasal axis post Cyto D treatment in cells pre-treated with the NF-κB inhibitor (**Figure 6E**, **Figure S6-B**) suggests that the increased filaments in the mid-cytoplasm arose from newly translated vimentin. Next, we explored whether Cyto D treatment led to an increase in the levels of intracellular ROS and further, whether the ROS was necessary to activate NF-κB. As expected, Cyto D treatment increased the intracellular ROS in NIH 3T3 cells (**Figure 6F**), which could be prevented by pre-treatment with vitamin C. Treatment of vitamin C alone neither altered the levels of intracellular ROS (**Figure 6F**) nor did it activate nuclear translocation of NF-κB (**Figure 6G-i and G-ii**). Vitamin C had a negligible effect on the density of vimentin filaments (Figure **S6-C**). Following that, we examined whether treatment of Cyto D in vitamin C pre-treated cells affected the transcription of vimentin. Despite the disassembly of actin filaments, the presence of vitamin C prevented Cyto D-mediated elevated expression of vimentin (**Figure 6H**). As expected, the presence of vitamin C prevented Cyto D-mediated increased assembly of vimentin filaments in the mid-cytoplasm (**Figure 6I**). This suggests that generation of ROS following the disruption of actin filaments is essential for the upregulation of vimentin in Cyto D treated cells. Interestingly, the elevation of ROS with H_2O_2 treatment led to a transcriptional (**Figure 6J**), as well as a translational (**Figure S6-G**) upregulation of vimentin (**Figure 6J**) and elevated density of the vimentin filaments across the apicobasal axis of cytoplasm (**Figure 6K and Figure S6-H**).

414

415 **Discussion**

416 The components of the eukaryotic cytoskeleton, including actin, microtubules, and
417 intermediate filaments, are interconnected, forming a complex meshwork of
418 biopolymers (Hohmann & Dehghani, 2019). This cytoskeletal meshwork is one of the
419 major regulators of the cytoplasmic mechanics (Fletcher & Mullins, 2010). The extent
420 to which the assembly and distribution of different cytoskeletal components are
421 interdependent, and their impact on the mechanical properties of the cytoplasm, is
422 incompletely understood and requires further investigation. Vimentin can control the
423 organisation of cortical actin in mitotic cells (Serres et al., 2020). Another study also
424 emphasizes the importance of the interaction between vimentin filaments and cortical
425 actin for normal cell division (Duarte et al., 2019). In our study, we observed that the
426 organisation of actin and microtubule filaments in interphase fibroblasts remained
427 unaffected by the knockout of vimentin (**Figure 4D** and **4E**). While the disassembly of
428 actin filaments by Cyto D did not affect the density of microtubules, it resulted in an
429 increased density of vimentin filaments in the mid-cytoplasm (**Figure 2D**), mediated
430 by ROS-dependent activation of NF-κB. Cyto D treatment of cells pre-treated with
431 either an NF-κB inhibitor (**Figure 6E-ii**) or a ROS quencher (**Figure 6I-ii**) prevented
432 the increase in vimentin filaments in the mid-cytoplasm. This suggests that the
433 disassembly of actin filaments alone does not trigger the assembly of vimentin
434 filaments and requires ROS as an essential component for the activation of NF-κB.
435 Nocodazole-induced disruption of microtubules did not affect the density of F-actin
436 (**Figure 3D** and **3E-i**). However, intriguingly, nocodazole treatment reduced the density
437 of vimentin filaments along the apicobasal axis (**Figure 3D** and **3E-iii**). Several reports
438 suggest the importance of microtubules in the proper assembly and dynamics of

439 vimentin filaments (Hookway et al., 2015; Prahlad et al., 1998). Therefore, we
440 conclude that nocodazole-induced microtubule disruption impairs the proper assembly
441 of vimentin filaments in NIH 3T3 fibroblasts. In U2OS cells, depletion of vimentin leads
442 to an increase in stress fibers in the basal cytoplasm, along with a mild increase in
443 actin monomers (Jiu et al., 2017). In contrast, depletion of vimentin in NIH 3T3
444 fibroblasts had a negligible effect on the stress fibres (**Figure 4D** and **4E-i**). This
445 suggests that the interdependence of the relative distribution of different cytoskeletal
446 components is cell type-dependent. Disassembly of actin by Cyto D caused a localised
447 increase in vimentin filaments in the mid-cytoplasm (**Figure 2D** and **2E-iii**). We show
448 that the localised assembly of vimentin in Cyto D-treated cells is dependent on the
449 cytoskeletal crosslinker protein plectin (**Figure 5I** and **S5-D**), suggesting that plectin
450 regulates the relative abundance of different cytoskeletal components in NIH 3T3
451 fibroblasts.

452 The rheological properties of the cytoplasm, specifically its stiffness (G') and fluidity
453 (η), are crucial for understanding cellular mechanics. In this manuscript, we investigate
454 the polarity of these rheological properties along the apicobasal axis. Cells situated
455 within a physically anisotropic extracellular microenvironment may exhibit distinct
456 behaviors in their basal and apical regions. By examining the polarity of cytoplasmic
457 stiffness and viscosity, we gain insights into how the mechanical properties of the
458 cytoplasm influence cellular sensing and respond to extracellular mechanical cues in
459 a heterogeneous 2D microenvironment. Furthermore, polarity in cytoplasmic stiffness
460 is expected to influence the organization and migration of cells within tissues. Previous
461 research has shown that fibroblast cells exhibit variable cytoplasmic stiffness at the
462 leading and trailing edges during migration (Ford & Rajagopalan, 2018). Cortical F-
463 actin is reported to enhance the stiffness of the cell cortex (Patteson et al., 2019). The

464 distribution of actin, vimentin, and microtubules in different regions of the cytoplasm is
465 inhomogeneous at macroscopic scales (**Figure 1H**). Thus, we speculate that the
466 rheological properties of different cytoplasmic regions are differentially affected by
467 various cytoskeletal filaments. Our study demonstrates that the anisotropic
468 organisation of these cytoskeletal filaments results in polarised cytoplasmic stiffness
469 and viscosity along the apicobasal axis in fibroblast cells cultured on glass substrate.
470 The significantly higher relative abundance of actin and vimentin filaments in the basal
471 cytoplasm (**Figure 1H**) suggests that these filaments likely govern the rheological
472 properties of the basal cytoplasm. Cyto D treatment reduced the stiffness (**Figure 2B**)
473 and increased the fluidity of the basal cytoplasm (**Figure S2A**) without altering the
474 abundance of microtubules and vimentin (**Figure 2D**). Interestingly, depletion of
475 vimentin (**Figure S4-A**) did not affect the abundance of actin or microtubule filaments
476 in the basal cytoplasm (**Figure 4D**). Additionally, treatment with nocodazole, which
477 disrupted both vimentin and microtubules in the basal cytoplasm (**Figure 3D**),
478 significantly decreased the elastic modulus, G' of the basal cytoplasm. This confirms
479 that actin and vimentin filaments jointly dictate the rheological properties of the basal
480 cytoplasm.

481 Longer actin filaments are absent in the mid-cytoplasm (**Figure 1G-i**). While we
482 anticipate a substantial decrease in the density of actin filaments in the mid-cytoplasm
483 compared to the basal cytoplasm in control cells, the FD of actin in the mid-cytoplasm
484 (1.58) shows only a slight reduction compared to that in the basal cytoplasm (1.72).
485 This smaller decrease in FD (**Figure 1H**) can be attributed to the presence of denser
486 actin filaments in the cell cortex. Consequently, the FD values do not accurately reflect
487 the actual density of F-actin in the perinuclear mid-cytoplasmic region. Therefore, we
488 expect the rheological properties of the mid-cytoplasm to be less dependent on actin

filaments and more influenced by vimentin and microtubules due to the absence of longer actin filaments. However, in Vim$^{-/-}$ cells, Cyto D treatment altered the rheological properties of the mid-cytoplasm without affecting microtubules (**Figure 4B** and **4C**). We speculate that these changes in the rheological properties of the mid-cytoplasm in Vim$^{-/-}$ cells following Cyto D treatment are due to alterations in the packing fraction of organelles (Gurel et al., 2014).

In cytoplasm where molecular motion of the cytoskeletal network is constrained by strong crosslinking and high filler content, a decrease in loss tangent with increasing frequency is expected, indicating reduced energy dissipation at higher frequencies. In contrast, an increase in loss tangent with frequency suggests a complex, time-dependent relaxation process, where energy dissipation mechanisms become more active at shorter time scales (higher frequencies). We infer that this behavior reflects the entanglement and weak crosslinking of cytoskeletal filaments. Since nocodazole treatment results in the loss of microtubules and a significant reduction in vimentin filaments while maintaining the density of actin filaments, we assume that the mechanical properties of the basal cytoplasm in nocodazole-treated cells are primarily governed by the actin filament network. The loss tangent of the basal cytoplasm in these cells resembles that of control cells, supporting our assumption. However, the loss tangent exhibits significantly different characteristics in the mid-cytoplasm (**Figure S3-C**). Therefore, we speculate that in nocodazole-treated cells, the mechanical properties of the mid-cytoplasm are not predominantly determined by cytoskeletal filaments but rather by the distribution of organelles. The comparable increase in compliance of the basal cytoplasm in control cells, as well as in vim$^{-/-}$ cells following Cyto D treatment (**Figure S4-D**), suggests that vimentin and actin filaments independently govern the mechanical characteristics of the basal cytoplasm.

515 **Materials and methods**

516 ***Cell culture***

517 NIH 3T3 fibroblast cells were obtained from NCCS, Pune, India. The cells were
518 cultured in DMEM media (Himedia, #AL007G) supplemented with 10% FBS (Himedia,
519 #RM10434) and 5% penicillin-streptomycin (Himedia, A001A) antibiotic cocktail
520 solution. The cells were consistently maintained at 37°C and 5% CO_2 inside a standard
521 cell culture incubator. Throughout the experiments, the cells were continuously
522 screened for mycoplasma contamination. For imaging purposes, cells were plated on
523 confocal dishes coated with poly-L-lysine (Sigma, #P8920) for maximum adherence,
524 ensuring that cell density never exceeded 60% confluency.

525 ***Drug treatment***

526 Cytochalasin D (Sigma, #C8273) was used at a concentration of 2 μM for 1 hour.
527 Nocodazole (Merck, #487928) was used at a concentration of 10 μM for 1 hour. NF-
528 κB inhibitor (CAY10512) was used at a concentration of 250 μM, 1 hour prior to the
529 addition of cytochalasin D. Vitamin C (Merck, A92902) was used at a concentration of
530 200 μM for 1 hour before treating with cytochalasin D. Cells were incubated with two
531 different concentrations (100 and 200 μM) of hydrogen peroxide (Merck, 107209)
532 solution for 15 minutes. Thereafter, the H_2O_2-containing media was replaced with
533 DMEM and the cells were further incubated for 40-60 minutes before carrying out
534 experiments.

535 ***Transfection***

536 The EGFP-p65 plasmid (Addgene plasmid #111190) was a gift from Johannes A.
537 Schmid (Schmid et al., 2000). Transfection was performed with FuGENE HD
538 (Promega, #E2311) transfection reagent according to the manufacturer's guidelines.

539 Cells were kept in serum-free DMEM for 12 hours prior to transfection. On the day of
540 transfection, the confluency of the cells was around 60-80%.

541 ***Knockdown of plectin***

542 Knockdown of plectin was performed using predesigned Dicer-substrate siRNA
543 (DsiRNA) from IDT (# mm.Ri.Plec.13.1). IDT negative control DsiRNA (# 51-01-14-03)
544 was used as a control siRNA. siRNAs were transfected into cells using FuGENE HD
545 (Promega, #E2311) transfection reagent according to the manufacturer's protocol.
546 Cells were incubated in siRNA-added media for a minimum of 72 hours to ensure
547 efficient depletion of plectin. The silencing of plectin was validated by western blot
548 analysis.

549 ***Knockout of vimentin using CRISPR-Cas9***

550 The vimentin knockout ($Vim^{-/-}$) NIH 3T3 cell line was generated using the CRISPR-
551 Cas9 technique. The guidelines for performing CRISPR-Cas9 mediated knockout
552 were adopted from the work published by Ran et al., 2013.(Ran et al., 2013). The
553 guide RNAs for vimentin were designed using the web-based CHOPCHOP tool
554 (Montague et al., 2014). The following oligos were used to construct the dual-stranded
555 guide RNA (gRNA) for vimentin:

Top strand (5'-3')	**CACC**GCGGAGCCACCGAACATCCTG
Bottom strand (5'-3')	**AAAC**CAGGATGTTCGGTGGCTCCGC

556

557 The bold letters denote the 5' overhangs required for ligation into the pSpCas9(BB)-
558 2A-Puro V2.0 vector plasmid. The remaining 21 nucleotides of the top strand
559 constitute the actual sequence of the gRNA: 5'-GCGGAGCCACCGAACATCCTG-3'.

560 The top and bottom strands were annealed together to create the dual-stranded
561 gRNA, which was then cloned into the pSpCas9(BB)-2A-Puro V2.0 vector plasmid
562 (Addgene ID #62988). The 5' overhangs of these oligos were phosphorylated using
563 T4 Polynucleotide Kinase (Thermo Scientific, #EK0031) to facilitate efficient ligation.
564 The annealing of these two oligos was performed in a thermocycler, gradually reducing
565 the temperature from 95°C to 25°C at a rate of 5°C per minute. Next, the gRNA
566 construct was cloned into the pSpCas9(BB)-2A-Puro V2.0 vector for co-expression
567 with Cas9. Prior to ligation, the pSpCas9(BB)-2A-Puro V2.0 vector was digested with
568 BpiI restriction endonuclease enzyme (Thermo Scientific, #ER1011) at 37°C for 1 hour.
569 There are two BpiI restriction sites in the pSpCas9(BB)-2A-Puro V2.0 vector. After
570 digestion, a fragment between these two sites is excised, and the gRNA construct is
571 inserted and ligated into the vector between these two sites. The ligation reaction was
572 performed by incubating the gRNA insert and the pSpCas9(BB)-2A-Puro V2.0 vector
573 at a ratio of 7:1 in the presence of T7 DNA ligase (New England Biolabs, # M0318S)
574 enzyme at 25°C for 1 hour. After successful cloning of the gRNA into the
575 pSpCas9(BB)-2A-Puro V2.0 vector, the entire construct was introduced into DH5α
576 strain of competent bacteria using the standard bacterial transformation protocol.
577 Following transformation, the bacteria were plated on Luria agar plates containing
578 ampicillin. Bacteria which were successfully transformed with pSpCas9(BB)-2A-Puro
579 V2.0 become resistant to ampicillin and gave rise to individual colonies. A few of these
580 colonies were picked for colony PCR to confirm the presence of the cloned
581 pSpCas9(BB)-2A-Puro V2.0 vector. Details of the primers used in the colony PCR is
582 given below,

Forward primer (5'-3') (U6 forward primer)	GAGGGCCTATTTCCCATGATT
Reverse primer (5'-3') (Bottom strand of the gRNA construct)	AAACCAGGATGTTCGGTGGCTCCGC

583

584 Following colony PCR, positive colonies were then plated onto another ampicillin-
585 containing agar plate. One or two colonies from this plate were then picked up and
586 grown in a liquid Luria broth culture medium at 37°C for overnight. The cloned gRNA
587 + pSpCas9(BB)-2A-Puro V2.0 constructs were then isolated from the bacterial culture
588 using a plasmid isolation kit (Macherey-Nagel, #740588.50). Following isolation, the
589 cloned constructs were transfected into NIH 3T3 cells using FuGENE HD (Promega,
590 #E2311) transfection reagent. pSpCas9(BB)-2A-Puro V2.0 plasmid contains
591 puromycin resistance gene. Next, the transfected cells were subjected to puromycin
592 (Sigma, #P8833) antibiotic treatment to isolate puromycin-resistant single-cell
593 colonies. These colonies were then screened for the presence of vimentin using
594 immunostaining and dot blot methods. Colonies with no vimentin expression were
595 isolated and subsequently used in the later experiments.

596 ***Western blotting***

597 For Western blot experiments, protein lysate of each sample was prepared from
598 approximately 3.2×10^6 cells seeded on a 60 mm cell culture dish. Cells were washed
599 three times with ice-cold PBS, then scraped and lysed in RIPA lysis buffer solution
600 supplemented with 1X protease and phosphatase inhibitor cocktail (Merck, PPC1010).
601 Protein concentrations were quantified using Bradford reagent. Blocking was
602 performed using 5% BSA solution (1 hour at room temperature) and the washes were

603 done using TBST buffer (Tris-buffered saline with 0.1% Tween 20). The antibodies
604 were diluted in 5% BSA solution. The following primary antibodies were used: vimentin
605 rabbit monoclonal antibody (dilution 1:1000; CST, #5741), β-tubulin rabbit polyclonal
606 antibody (dilution 1:1000, Abclonal, #AC008), β-actin mouse monoclonal antibody
607 (dilution 1:1000, SCBT, #sc-47778), GAPDH mouse monoclonal antibody (dilution
608 1:2000, Abclonal, #AC002), NF-κB p65 (L8F6) mouse monoclonal antibody (dilution
609 1:1000; CST, #6956), plectin mouse monoclonal antibody (dilution 1:500; SCBT, #sc-
610 33469), histone H3 rabbit polyclonal antibody (dilution 1:1000; Invitrogen, # PA5-
611 16183). The following horseradish peroxidase (HRP)-tagged secondary antibodies
612 were used: anti-mouse secondary antibody (dilution 1:10000; Invitrogen, #31430) and
613 anti-rabbit secondary antibody (dilution 1:10000; Invitrogen, #31460).
614 Chemiluminescent signals from were developed by incubating the blots in a substrate
615 solution containing luminol, coumaric acid, and H_2O_2, prepared in 1.5M Tris-HCl buffer
616 (pH 8.8), for 30-40 seconds. The band intensities were quantified using ImageJ. The
617 intensity ratios of the total protein to the loading control GAPDH were calculated.

618 ***Protein isolation from nuclear and cytoplasmic fractions***

619 Cells were harvested using a scraper after three washes with ice-cold PBS. The cell
620 pellet was then resuspended in approximately 500 μl of cytoplasmic extraction buffer,
621 supplemented with 0.05% NP-40 detergent. The samples were vortexed frequently to
622 separate the nuclear fraction from the cytoplasmic fraction. Subsequently, the samples
623 were centrifuged at 10,000 × g and 4°C for 15 minutes, and the supernatant,
624 containing the cytoplasmic fraction, was collected. The remaining pellet was
625 resuspended in 400 μl of nuclear extraction buffer and vortexed every few minutes for
626 40 minutes to lyse the nuclear membrane. Finally, the samples were centrifuged at

627 15,000 × g and 4°C for 15 minutes, and the supernatant, containing the nuclear protein
628 fraction, was collected.

629 ***Cell fixation and immunostaining***

630 For immunostaining, cells were seeded on glass-bottom confocal dishes coated with
631 either poly-L-lysine or fibronectin solution for optimal adhesion. The confluency of the
632 seeded cells was kept below 70%. Following various drug treatments, cells were fixed
633 in 4% PFA solution and permeabilized using 0.1% Triton X-100 in PBS. Blocking was
634 performed using 2% BSA solution in PBS for 1 hour at room temperature. Cells were
635 incubated with the following primary antibody solutions for 16 hours at 4°C: vimentin
636 anti-rabbit monoclonal antibody (dilution 1:100; Cell Signalling Technology, #5741) and
637 β-tubulin rabbit polyclonal antibody (dilution 1:200; Abclonal, #AC008). Alexa Fluor
638 488 and 594-tagged anti-rabbit secondary antibodies (CST) were used at a 1:500
639 dilution. F-actin was visualised using Alexa Fluor 488 conjugated phalloidin (dilution
640 1:200, Invitrogen, # A12379).

641 ***qPCR analysis***

642 The total RNA from NIH 3T3 cells was extracted using RNeasy mini kit (Qiagen,
643 #74104). cDNA was synthesised from the RNA samples using Verso cDNA synthesis
644 kit (Thermo Scientific, #AB1453A). qPCR was performed using Genious 2X SYBR
645 Green Fast qPCR Mix (Abclonal, #RK21204) in an Applied Biosystems 7500 Fast
646 Real-Time PCR system. The sequences of the primers used for the qPCR are
647 provided in the table below,

Vimentin	Forward (5'-3')	ATGCGGCTGCGAGAGAAATTG
	Reverse (5'-3')	TCAAGACGTGCCAGAGAAGCA

GAPDH	Forward (5'-3')	CAGGAGAGTGTTTCCTCGTCC
	Reverse (5'-3')	ATGAAGGGGTCGTTGATGGC

648

649 GAPDH was used as the housekeeping gene to normalise the expression levels of
650 vimentin.

651 ***Measurement of ROS***

652 Intracellular ROS levels under various conditions were quantified using DCFDA
653 (Merck) solution. Cells were seeded on a 96-well plate at a density of approximately
654 25000 cells per well and allowed to adhere properly for overnight. Thereafter, the cells
655 in each well were incubated with 100μL of DCFDA (20 μM) solution prepared in serum-
656 free DMEM media for 1 hour. Next, the DCFDA solution was washed out, and the cells
657 were treated with the desired drug solutions (prepared in DMEM) for the appropriate
658 duration. Subsequently, the fluorescence intensity of DCFDA was measured using a
659 fluorescence plate reader (Ex/Em = 485/535 nm). The fluorescent intensity correlates
660 with ROS levels.

661 ***Microscopy and image analysis***

662 Immunofluorescent images of actin, vimentin, and microtubule filaments were
663 captured using a Zeiss LSM 880 confocal microscope with a 63X (NA 1.4) oil
664 immersion objective (Zeiss, Thornwood, NY). Z-stack images were captured with an
665 interval of 0.45 μm between each slice. To minimize cell-to-cell variation, cells with
666 similar heights were selected, maintaining a consistent number of z-slices (8-10) for
667 each cell. Fluorescent images of cells expressing EGFP-p65 were captured using a
668 Zeiss AXIO Observer.Z1 wide-field epifluorescence microscope with a 63X oil
669 immersion objective. Live cell imaging was performed on a heated microscope stage

670 (+37°C) in presence of 5% CO_2. Images were acquired using either Zen 2.0 or
671 μManager software. Calculation of nuclear-to-cytoplasmic (N/C) intensity ratios of
672 EGFP-p65 was carried out by selecting regions of interest (ROIs) from cytoplasmic
673 and nuclear regions, and their mean intensity values were quantified using ImageJ.

674 ***Fractal dimension analysis***

675 Fractal dimension (FD) values of the actin, vimentin, and microtubule filaments were
676 calculated using the FracLac (v2.5) plugin (Karperien, 1999) for ImageJ. 16-bit
677 confocal images were converted into 8-bit binary images. Thresholding was performed
678 using the Otsu method. During thresholding, efforts were made to ensure maximum
679 visibility of cytoskeletal filaments while minimising background noise.

680 ***Particle tracking microrheology (PTM)***

681 The entire procedure of PTM was conducted as described in the standard protocol
682 (Tseng et al., 2002; Wirtz, 2009). Fluorescently tagged carboxylate modified
683 microspheres (Invitrogen, #F8811) having diameter of 200nm were ballistically shot
684 inside the cell using a gene gun system (Bio-Rad, Helios® Gene gun system). After
685 the shooting, the cells were washed with 1X PBS solution to wash away unbound
686 beads and detached cells. The cells were then kept in a cell culture incubator under
687 standard conditions (37°C, 5% CO_2) for 16 hours in serum-free DMEM medium to
688 allow healing from the injuries caused by the shooting of the microspheres. The cells
689 containing fluorescent microspheres were subsequently positioned on the microscope
690 stage at 37°C. The movements of the microspheres were recorded in the form of
691 movies using a high-speed Hamamatsu Orca Flash 4.0 CMOS camera and μManager
692 software (A. Edelstein et al., 2010; A. D. Edelstein et al., 2014). Each movie comprised
693 1000 frames, spanning a total duration of 20 seconds, with an exposure time of 20

milliseconds. The trajectories of the microspheres were extracted by tracking their movements using the MOSAICsuite plugin (Sbalzarini & Koumoutsakos, 2005) of ImageJ. At least 5-10 beads from each cell were tracked to obtain the rheological properties of the cytoplasm. The Mean Squared Displacement (MSD) and compliance (Γ) values were computed from these trajectories using a MATLAB script. MSDs having slopes greater than 1 were filtered out. While the movement of the microspheres was recorded for 1000 frames, only the first 250 frames were considered for calculating the MSDs to avoid potential errors from later data points in the trajectories. Subsequently, the complex shear modulus (G*(ω)), viscous modulus (G''), and elastic modulus (G') were derived from the MSDs using another MATLAB script.

Acknowledgements

DR would like to thank Mahesh Agarwal and Parijat Biswas for their valuable insights into the principles and methodology of particle tracking microrheology. Special thanks to Mrs. Debapriya Ghatak for her assistance with the confocal microscopy.

Funding

DKS was supported by grants received from Department of Science and Technology, Ministry of Science and Technology, India (DST, Grant #**SB/S0/BB-101/2013**), Department of Biotechnology, Ministry of Science and Technology, India (DBT, Grant #**BT/PR6995/BRB/10/1140/2012**), and IACS. DR was supported by fellowship received from Council of Scientific and Industrial Research (CSIR) via file number **09/080(1134)/2019-EMR-I**.

Author contributions

DKS: Conceptualisation, Funding acquisition, Resources, Supervision, Writing – original draft, Writing – reviewing and editing. **DR**: Conceptualisation, performed

experiments, data analysis, data interpretation, wrote MATLAB scripts, Writing - reviewing and editing, preparation of figures.

Competing interests

The authors declare no competing or financial interests.

References

1. Bausch, A. R., Ziemann, F., Boulbitch, A. A., Jacobson, K., & Sackmann, E. (1998). Local measurements of viscoelastic parameters of adherent cell surfaces by magnetic bead microrheometry. *Biophysical Journal*, *75*(4), 2038–2049. https://doi.org/10.1016/S0006-3495(98)77646-5

2. Bray, D. (2000). *Cell Movements: From Molecules to Motility* (2nd ed.). Garland Science. https://doi.org/10.4324/9780203833582

3. Brown, S. S., & Spudich, J. A. (1981). Mechanism of action of cytochalasin: Evidence that it binds to actin filament ends. *The Journal of Cell Biology*, *88*(3), 487–491. https://doi.org/10.1083/jcb.88.3.487

4. Casella, J. F., Flanagan, M. D., & Lin, S. (1981). Cytochalasin D inhibits actin polymerization and induces depolymerization of actin filaments formed during platelet shape change. *Nature*, *293*(5830), 302–305. https://doi.org/10.1038/293302a0

5. Cooper, J. A. (1987). Effects of cytochalasin and phalloidin on actin. *The Journal of Cell Biology*, *105*(4), 1473–1478. https://doi.org/10.1083/jcb.105.4.1473

6. Duarte, S., Viedma-Poyatos, Á., Navarro-Carrasco, E., Martínez, A. E., Pajares, M. A., & Pérez-Sala, D. (2019). Vimentin filaments interact with the actin cortex in mitosis allowing normal cell division. *Nature Communications*, *10*(1), 4200. https://doi.org/10.1038/s41467-019-12029-4

7. Edelstein, A., Amodaj, N., Hoover, K., Vale, R., & Stuurman, N. (2010). Computer Control of Microscopes Using µManager. *Current Protocols in Molecular Biology*, *92*(1). https://doi.org/10.1002/0471142727.mb1420s92

8. Edelstein, A. D., Tsuchida, M. A., Amodaj, N., Pinkard, H., Vale, R. D., & Stuurman, N. (2014). Advanced methods of microscope control using µManager software. *Journal of Biological Methods*, *1*(2), e10. https://doi.org/10.14440/jbm.2014.36

9. Ellis, R. J. (2001). Macromolecular crowding: Obvious but underappreciated. *Trends in Biochemical Sciences*, *26*(10), 597–604. https://doi.org/10.1016/s0968-0004(01)01938-7

10. Fels, J., Orlov, S. N., & Grygorczyk, R. (2009). The hydrogel nature of mammalian cytoplasm contributes to osmosensing and extracellular pH sensing. *Biophysical Journal*, *96*(10), 4276–4285. https://doi.org/10.1016/j.bpj.2009.02.038

11. Fletcher, D. A., & Mullins, R. D. (2010). Cell mechanics and the cytoskeleton. *Nature*, *463*(7280), 485–492. https://doi.org/10.1038/nature08908

12. Ford, A. J., & Rajagopalan, P. (2018). Measuring Cytoplasmic Stiffness of Fibroblasts as a Function of Location and Substrate Rigidity Using Atomic Force Microscopy. *ACS Biomaterials Science & Engineering*, *4*(12), 3974–3982. https://doi.org/10.1021/acsbiomaterials.8b01019

13. Guigas, G., Kalla, C., & Weiss, M. (2007). Probing the nanoscale viscoelasticity of intracellular fluids in living cells. *Biophysical Journal*, *93*(1), 316–323. https://doi.org/10.1529/biophysj.106.099267

14. Gurel, P. S., Hatch, A. L., & Higgs, H. N. (2014). Connecting the Cytoskeleton to the Endoplasmic Reticulum and Golgi. *Current Biology*, *24*(14), R660–R672. https://doi.org/10.1016/j.cub.2014.05.033

15. Hohmann, T., & Dehghani, F. (2019). The Cytoskeleton-A Complex Interacting Meshwork. *Cells*, *8*(4), 362. https://doi.org/10.3390/cells8040362

16. Hookway, C., Ding, L., Davidson, M. W., Rappoport, J. Z., Danuser, G., & Gelfand, V. I. (2015). Microtubule-dependent transport and dynamics of vimentin intermediate filaments. *Molecular Biology of the Cell*, *26*(9), 1675–1686. https://doi.org/10.1091/mbc.E14-09-1398

17. Hu, J., Jafari, S., Han, Y., Grodzinsky, A. J., Cai, S., & Guo, M. (2017). Size- and speed-dependent mechanical behavior in living mammalian cytoplasm. *Proceedings of the*

National Academy of Sciences of the United States of America, *114*(36), 9529–9534. https://doi.org/10.1073/pnas.1702488114

18. Jiu, Y., Peränen, J., Schaible, N., Cheng, F., Eriksson, J. E., Krishnan, R., & Lappalainen, P. (2017). Vimentin intermediate filaments control actin stress fiber assembly through GEF-H1 and RhoA. *Journal of Cell Science*, *130*(5), 892–902. https://doi.org/10.1242/jcs.196881

19. Karperien, A. (1999). *FracLac for ImageJ*. https://imagej.net/ij/plugins/fraclac/FLHelp/Introduction.htm

20. Kustermans, G., El Benna, J., Piette, J., & Legrand-Poels, S. (2005). Perturbation of actin dynamics induces NF-kappaB activation in myelomonocytic cells through an NADPH oxidase-dependent pathway. *The Biochemical Journal*, *387*(Pt 2), 531–540. https://doi.org/10.1042/BJ20041318

21. Liu, C.-Y., Lin, H.-H., Tang, M.-J., & Wang, Y.-K. (2015). Vimentin contributes to epithelial-mesenchymal transition cancer cell mechanics by mediating cytoskeletal organization and focal adhesion maturation. *Oncotarget*, *6*(18), 15966–15983. https://doi.org/10.18632/oncotarget.3862

22. Maninová, M., & Vomastek, T. (2016). Dorsal stress fibers, transverse actin arcs, and perinuclear actin fibers form an interconnected network that induces nuclear movement in polarizing fibroblasts. *The FEBS Journal*, *283*(20), 3676–3693. https://doi.org/10.1111/febs.13836

23. Marks, P. C., Hewitt, B. R., Baird, M. A., Wiche, G., & Petrie, R. J. (2022). Plectin linkages are mechanosensitive and required for the nuclear piston mechanism of three-dimensional cell migration. *Molecular Biology of the Cell*, *33*(12), ar104. https://doi.org/10.1091/mbc.E21-08-0414

24. Marsigliante, S., Vetrugno, C., & Muscella, A. (2016). Paracrine CCL20 loop induces epithelial-mesenchymal transition in breast epithelial cells. *Molecular Carcinogenesis*, *55*(7), 1175–1186. https://doi.org/10.1002/mc.22360

25. Masiello, N. C., Zucker, M. B., Casella, J. F., Flanagan, M. D., & Lin, S. (1982). Effect of cytochalasin D on thrombin-induced actin filaments in platelets. *Nature*, *298*(5870), 202. https://doi.org/10.1038/298202b0

26. Mason, T. G. (2000). Estimating the viscoelastic moduli of complex fluids using the generalized Stokes-Einstein equation. *Rheologica Acta*, *39*(4), 371–378. https://doi.org/10.1007/s003970000094

27. Mendez, M. G., Restle, D., & Janmey, P. A. (2014). Vimentin enhances cell elastic behavior and protects against compressive stress. *Biophysical Journal*, *107*(2), 314–323. https://doi.org/10.1016/j.bpj.2014.04.050

28. Moeendarbary, E., Valon, L., Fritzsche, M., Harris, A. R., Moulding, D. A., Thrasher, A. J., Stride, E., Mahadevan, L., & Charras, G. T. (2013). The cytoplasm of living cells behaves as a poroelastic material. *Nature Materials*, *12*(3), 253–261. https://doi.org/10.1038/nmat3517

29. Montague, T. G., Cruz, J. M., Gagnon, J. A., Church, G. M., & Valen, E. (2014). CHOPCHOP: A CRISPR/Cas9 and TALEN web tool for genome editing. *Nucleic Acids Research*, *42*(Web Server issue), W401-407. https://doi.org/10.1093/nar/gku410

30. Morgan, M. J., & Liu, Z. (2011). Crosstalk of reactive oxygen species and NF-κB signaling. *Cell Research*, *21*(1), 103–115. https://doi.org/10.1038/cr.2010.178

31. Munder, M. C., Midtvedt, D., Franzmann, T., Nüske, E., Otto, O., Herbig, M., Ulbricht, E., Müller, P., Taubenberger, A., Maharana, S., Malinovska, L., Richter, D., Guck, J., Zaburdaev, V., & Alberti, S. (2016). A pH-driven transition of the cytoplasm from a fluid- to a solid-like state promotes entry into dormancy. *eLife*, *5*, e09347. https://doi.org/10.7554/eLife.09347

32. Najafi, J., Dmitrieff, S., & Minc, N. (2023). Size- and position-dependent cytoplasm viscoelasticity through hydrodynamic interactions with the cell surface. *Proceedings of the National Academy of Sciences of the United States of America*, *120*(9), e2216839120. https://doi.org/10.1073/pnas.2216839120

33. Patteson, A. E., Pogoda, K., Byfield, F. J., Mandal, K., Ostrowska-Podhorodecka, Z., Charrier, E. E., Galie, P. A., Deptuła, P., Bucki, R., McCulloch, C. A., & Janmey, P. A. (2019). Loss of Vimentin Enhances Cell Motility through Small Confining Spaces. *Small (Weinheim an Der Bergstrasse, Germany)*, *15*(50), e1903180. https://doi.org/10.1002/smll.201903180

34. Pegoraro, A. F., Janmey, P., & Weitz, D. A. (2017). Mechanical Properties of the Cytoskeleton and Cells. *Cold Spring Harbor Perspectives in Biology*, *9*(11), a022038. https://doi.org/10.1101/cshperspect.a022038

35. Pollard, T. D. (1976). The role of actin in the temperature-dependent gelation and contraction of extracts of Acanthamoeba. *The Journal of Cell Biology*, *68*(3), 579–601. https://doi.org/10.1083/jcb.68.3.579

36. Prahlad, V., Yoon, M., Moir, R. D., Vale, R. D., & Goldman, R. D. (1998). Rapid movements of vimentin on microtubule tracks: Kinesin-dependent assembly of intermediate filament networks. *The Journal of Cell Biology*, *143*(1), 159–170. https://doi.org/10.1083/jcb.143.1.159

37. Ran, F. A., Hsu, P. D., Wright, J., Agarwala, V., Scott, D. A., & Zhang, F. (2013). Genome engineering using the CRISPR-Cas9 system. *Nature Protocols*, *8*(11), 2281–2308. https://doi.org/10.1038/nprot.2013.143

38. Rotsch, C., & Radmacher, M. (2000). Drug-Induced Changes of Cytoskeletal Structure and Mechanics in Fibroblasts: An Atomic Force Microscopy Study. *Biophysical Journal*, *78*(1), 520–535. https://doi.org/10.1016/S0006-3495(00)76614-8

39. Sanchez, A. D., & Feldman, J. L. (2017). Microtubule-organizing centers: From the centrosome to non-centrosomal sites. *Current Opinion in Cell Biology*, *44*, 93–101. https://doi.org/10.1016/j.ceb.2016.09.003

40. Sarria, A. J., Nordeen, S. K., & Evans, R. M. (1990). Regulated expression of vimentin cDNA in cells in the presence and absence of a preexisting vimentin filament network. *The Journal of Cell Biology*, *111*(2), 553–565. https://doi.org/10.1083/jcb.111.2.553

41. Sbalzarini, I. F., & Koumoutsakos, P. (2005). Feature point tracking and trajectory analysis for video imaging in cell biology. *Journal of Structural Biology*, *151*(2), 182–195. https://doi.org/10.1016/j.jsb.2005.06.002

42. Schmid, J. A., Birbach, A., Hofer-Warbinek, R., Pengg, M., Burner, U., Furtmüller, P. G., Binder, B. R., & de Martin, R. (2000). Dynamics of NF kappa B and Ikappa Balpha studied with green fluorescent protein (GFP) fusion proteins. Investigation of GFP-p65 binding to DNa by fluorescence resonance energy transfer. *The Journal of Biological Chemistry*, *275*(22), 17035–17042. https://doi.org/10.1074/jbc.M000291200

43. Schuh, M., & Ellenberg, J. (2007). Self-Organization of MTOCs Replaces Centrosome Function during Acentrosomal Spindle Assembly in Live Mouse Oocytes. *Cell*, *130*(3), 484–498. https://doi.org/10.1016/j.cell.2007.06.025

44. Schwarzl, F. R. (1971). Numerical calculation of storage and loss modulus from stress relaxation data for linear viscoelastic materials. *Rheologica Acta*, *10*(2), 165–173. https://doi.org/10.1007/BF02040437

45. Serres, M. P., Samwer, M., Truong Quang, B. A., Lavoie, G., Perera, U., Görlich, D., Charras, G., Petronczki, M., Roux, P. P., & Paluch, E. K. (2020). F-Actin Interactome Reveals Vimentin as a Key Regulator of Actin Organization and Cell Mechanics in Mitosis. *Developmental Cell*, *52*(2), 210-222.e7. https://doi.org/10.1016/j.devcel.2019.12.011

46. Svitkina, T. M. (2020). Actin Cell Cortex: Structure and Molecular Organization. *Trends in Cell Biology*, *30*(7), 556–565. https://doi.org/10.1016/j.tcb.2020.03.005

47. Svitkina, T. M., Verkhovsky, A. B., & Borisy, G. G. (1996). Plectin sidearms mediate interaction of intermediate filaments with microtubules and other components of the cytoskeleton. *The Journal of Cell Biology*, *135*(4), 991–1007. https://doi.org/10.1083/jcb.135.4.991

48. Tojkander, S., Gateva, G., & Lappalainen, P. (2012). Actin stress fibers – assembly, dynamics and biological roles. *Journal of Cell Science*, jcs.098087. https://doi.org/10.1242/jcs.098087

49. Trevors, J. T. (2011). The Composition and Organization of Cytoplasm in Prebiotic Cells. *International Journal of Molecular Sciences*, *12*(3), 1650–1659. https://doi.org/10.3390/ijms12031650

50. Tseng, Y., Kole, T. P., & Wirtz, D. (2002). Micromechanical Mapping of Live Cells by Multiple-Particle-Tracking Microrheology. *Biophysical Journal*, *83*(6), 3162–3176. https://doi.org/10.1016/S0006-3495(02)75319-8

51. Wiche, G. (1998). Role of plectin in cytoskeleton organization and dynamics. *Journal of Cell Science*, *111*(17), 2477–2486. https://doi.org/10.1242/jcs.111.17.2477

52. Wirtz, D. (2009). Particle-tracking microrheology of living cells: Principles and applications. *Annual Review of Biophysics*, *38*, 301–326. https://doi.org/10.1146/annurev.biophys.050708.133724

53. Xie, J., Najafi, J., Le Borgne, R., Verbavatz, J.-M., Durieu, C., Sallé, J., & Minc, N. (2022). Contribution of cytoplasm viscoelastic properties to mitotic spindle positioning. *Proceedings of the National Academy of Sciences of the United States of America*, *119*(8), e2115593119. https://doi.org/10.1073/pnas.2115593119

54. Xu, K., Schwarz, P. M., & Ludueña, R. F. (2002). Interaction of nocodazole with tubulin isotypes. *Drug Development Research*, *55*(2), 91–96. https://doi.org/10.1002/ddr.10023

55. Zhang, Y., Zhao, S., Li, M., Li, Y., Feng, F., Cui, J., Xue, Y., Jin, X., & Jiu, Y. (2021). *Host cytoskeletal vimentin serves as a structural organizer and an RNA-binding protein regulator to facilitate Zika viral replication*. https://doi.org/10.1101/2021.04.25.441301

56. Zhou, H., Xu, J., Zhang, C., & Wen, Y. (2019). Aberrant histone deacetylase 1 expression upregulates vimentin expression via an NF-κB-dependent pathway in hepatocellular carcinoma. *Oncology Letters*. https://doi.org/10.3892/ol.2019.10309

57. Zimmerman, S. B., & Minton, A. P. (1993). Macromolecular crowding: Biochemical, biophysical, and physiological consequences. *Annual Review of Biophysics and*

Biomolecular Structure, *22*, 27–65. https://doi.org/10.1146/annurev.bb.22.060193.000331

Figures with legends

Figure 1

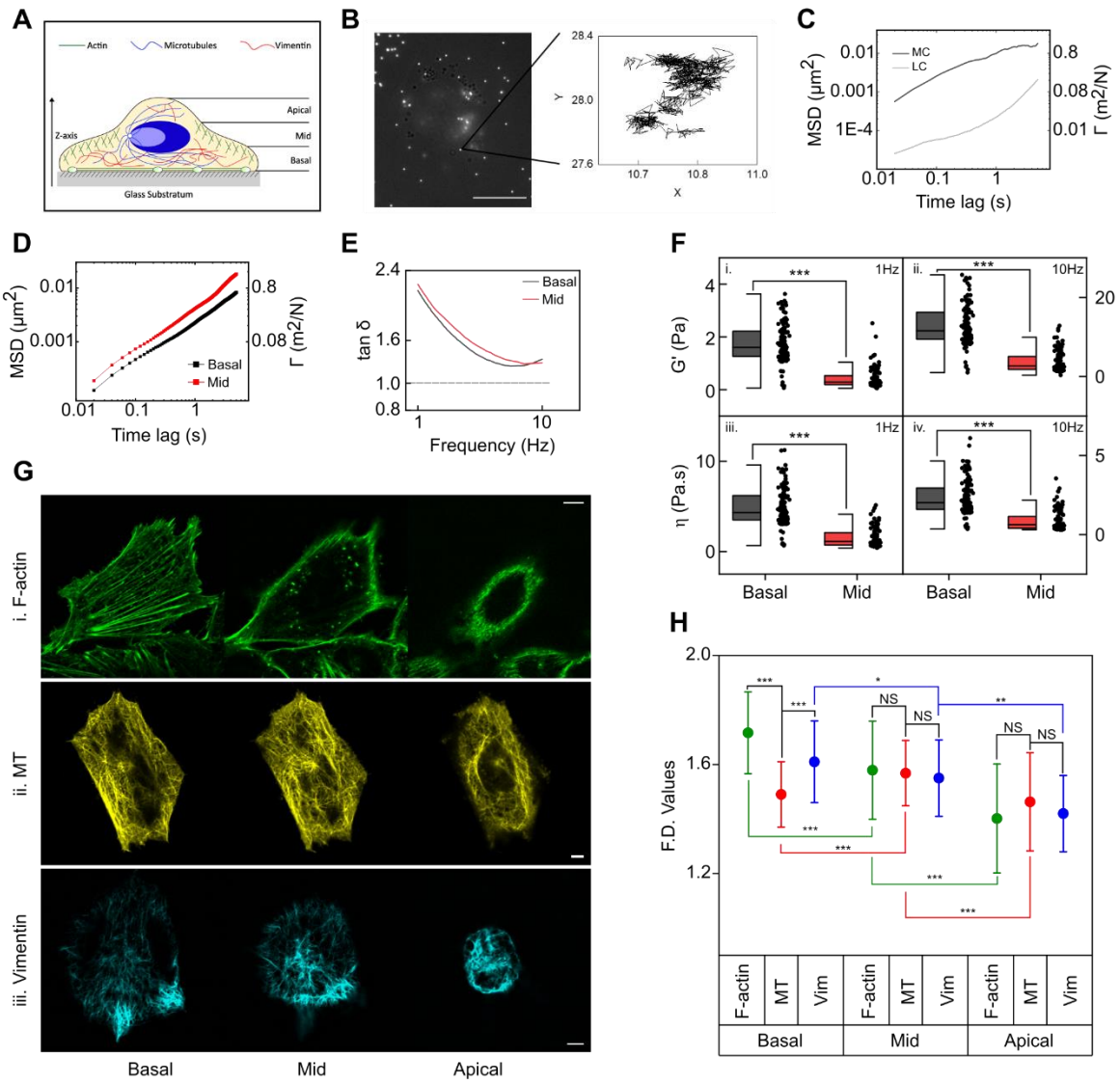

Figure 1: Mechanical properties of the cytoplasm are polarised along the apicobasal axis. (**A**) Cartoon of a cell illustrating the distribution of actin, microtubule, and vimentin filaments, along with segmentation of the cytoplasm into basal, mid, and apical regions along the z-axis. (**B**) Fluorescently labelled microspheres with a diameter of 200 nm dispersed throughout the cytoplasm of an NIH 3T3 fibroblast (Scale bar, 5 μm). (Inset) Trajectory of one such microsphere tracked over a 20-second

period. (**C**) MSD (left axis) and compliance, Γ (right axis) of the most compliant (MC) and least compliant (LC) regions within the cytoplasm of a specific cell. (**D**) Mean MSD (left axis) and compliance, Γ (right axis) of the basal and mid cytoplasmic regions. (N_{beads} > 80, N_{cells} > 15) (**E**) Loss tangent profiles of the basal and mid cytoplasmic regions. (**F**) Comparison of elastic modulus (G') values between the basal and mid cytoplasmic regions at 1 Hz (i) and 10 Hz (ii) frequencies. Comparison of dynamic viscosity (η) values between the basal and mid cytoplasm at 1 Hz (iii) and 10 Hz (iv) frequencies. (N_{beads} > 80, N_{cells} > 15; ***p<0.001, Mann-Whitney U test) (**G**) Representative confocal images of F-actin (i), microtubule, MT (ii) and vimentin filaments (iii) across the basal, mid and apical cytoplasm. (Scale bar, 5 μm) (**H**) Fractal dimension (FD) values of actin, microtubule (MT) and vimentin (Vim) filaments across the apicobasal axis. (Mean ± SD, N_{cells} > 100; *p<0.05, **p<0.01, ***p<0.001, NS, non-significant, two sample T-test)

937 **Figure 2**

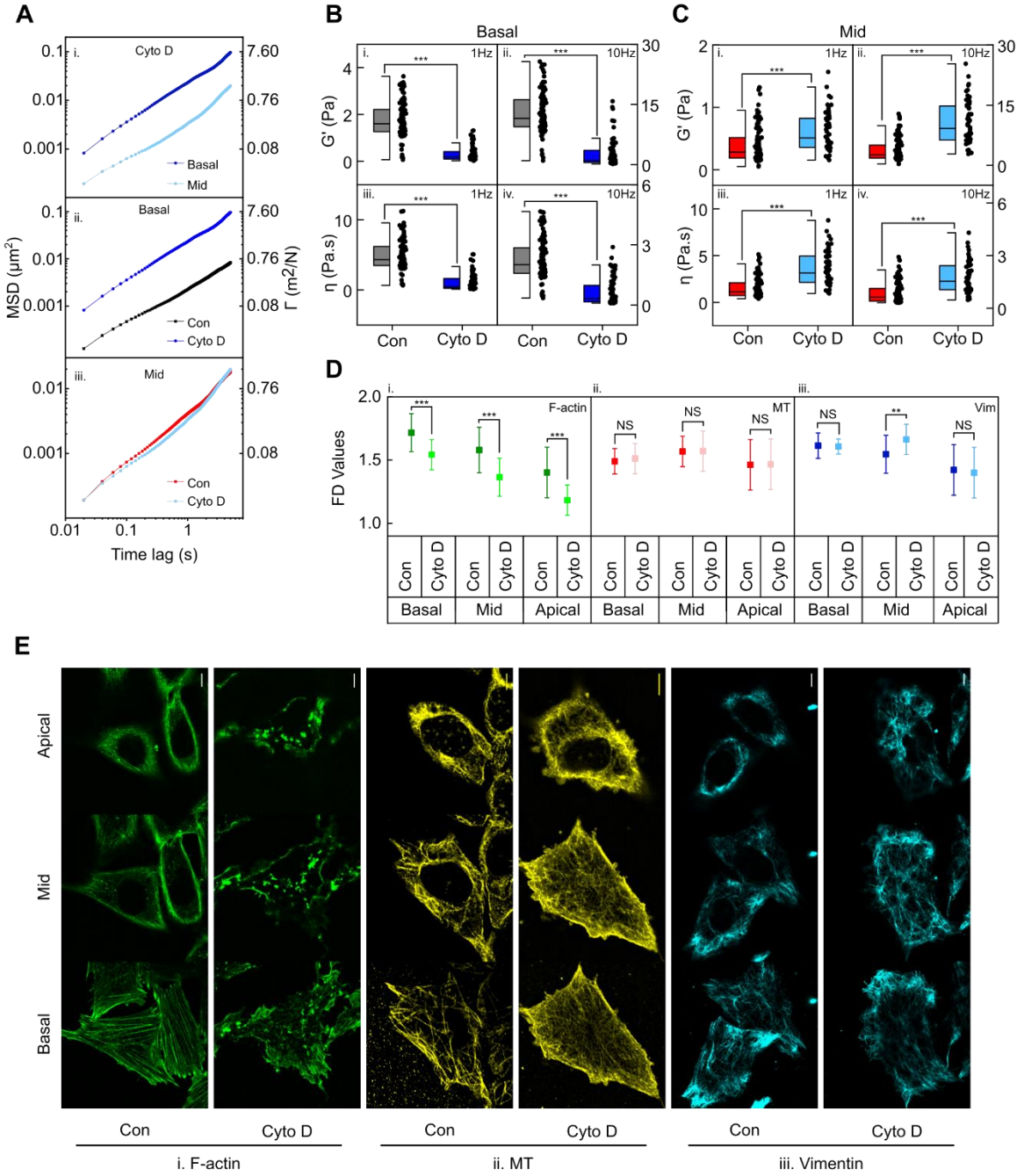

938

939 **Figure 2: Disruption of actin filaments has contrasting effects on the mechanical**

940 **properties of the basal and mid cytoplasm.** (**A**) Mean MSD (left axis) and

941 compliance, Γ (right axis) of the basal and mid cytoplasmic regions of Cyto D treated

942 cells (i), comparison of Mean MSDs (left axis) and compliance, Γ (right axis) between

943 the control and Cyto D treated cells across the basal (ii) and mid (iii) cytoplasmic
944 regions. (N_{beads} > 80, N_{cells} > 15) (**B**) Comparison of elastic moduli (G') between the
945 control and Cyto D treated cells across the basal cytoplasmic region at 1 Hz (i) and 10
946 Hz (ii) frequencies. Comparison of dynamic viscosity (η) values between the control
947 and Cyto D treated cells across the basal cytoplasmic region at 1 Hz (iii) and 10 Hz
948 (iv) frequencies. (N_{beads} > 80, N_{cells} > 15; ***p<0.001, Mann-Whitney U test) (**C**)
949 Comparison of elastic moduli (G') between the control and Cyto D treated cells across
950 the mid cytoplasmic region at 1 Hz (i) and 10 Hz (ii) frequencies. Comparison of
951 dynamic viscosity (η) values between the control and Cyto D treated cells across the
952 mid cytoplasmic region at 1 Hz (iii) and 10 Hz (iv) frequencies. (N_{beads} > 80, N_{cells} > 15;
953 ***p<0.001, Mann-Whitney U test) (**D**) Fractal dimension (FD) values of actin,
954 microtubule (MT) and vimentin filaments in control and Cyto D treated cells across the
955 apicobasal axis. (Mean ± SD, N_{cells} > 100; **p<0.01, ***p<0.001, NS, non-significant,
956 two sample T-test) (**E**) Representative confocal images of F-actin, microtubules (MT)
957 and vimentin filaments in the control and Cyto D treated cells across the apicobasal
958 axis. (Scale bar, 5 μm)

959

960 **Figure 3**

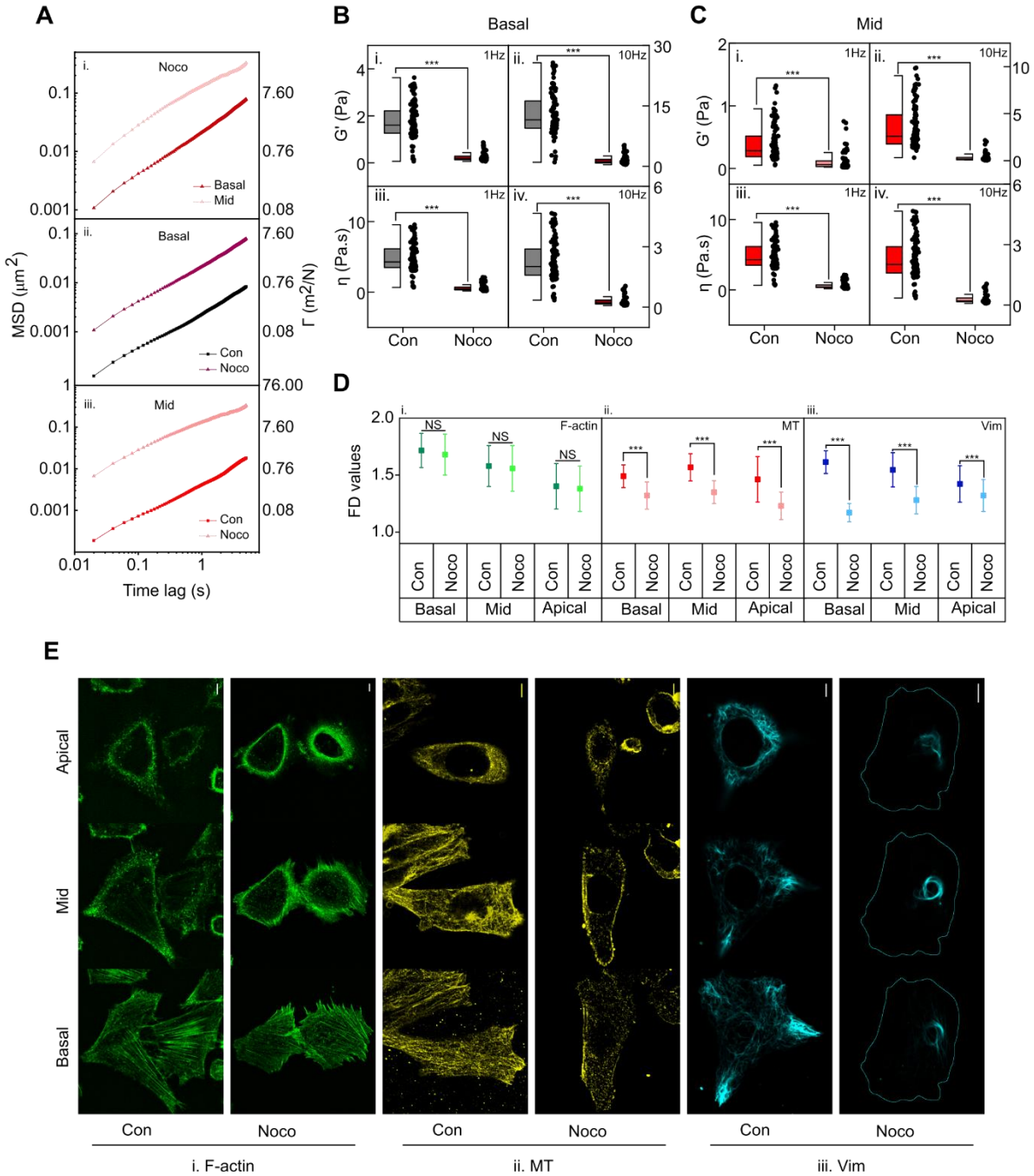

961

962 **Figure 3: Nocodazole-induced depolymerization of microtubules results in**
963 **significant softening of the cytoplasm across the apicobasal axis.** (**A**) Mean MSD
964 (left axis) and compliance, Γ (right axis) of the basal and mid cytoplasmic regions of
965 nocodazole (noco) treated cells (i), comparison of Mean MSDs (left axis) and

compliance, Γ (right axis) between the control and nocodazole treated cells across the basal (ii) and mid (iii) cytoplasmic regions. (N_{beads} > 60, N_{cells} > 10) (**B**) Comparison of elastic moduli (G') between the control and nocodazole treated cells across the basal cytoplasmic region at 1 Hz (i) and 10 Hz (ii) frequencies. Comparison of dynamic viscosity (η) values between the control and nocodazole treated cells across the basal cytoplasmic region at 1 Hz (iii) and 10 Hz (iv) frequencies. (N_{beads} > 60, N_{cells} > 10; ***p<0.001, Mann-Whitney U test) (**C**) Comparison of elastic moduli (G') between the control and nocodazole treated cells across the mid cytoplasmic region at 1 Hz (i) and 10 Hz (ii) frequencies. Comparison of dynamic viscosity (η) values between the control and nocodazole treated cells across the mid cytoplasmic region at 1 Hz (iii) and 10 Hz (iv) frequencies. (N_{beads} > 60, N_{cells} > 10; ***p<0.001, Mann-Whitney U test) (**D**) Fractal dimension (FD) values of actin, microtubule (MT) and vimentin filaments in control and nocodazole treated cells across the apicobasal axis. (Mean ± SD, N_{cells} > 100; ***p<0.001, NS, non-significant, two sample T-test) (**E**) Representative confocal images of F-actin, microtubules (MT) and vimentin filaments in the control and nocodazole treated cells across the apicobasal axis. (Scale bar, 5 μm)

983 **Figure 4**

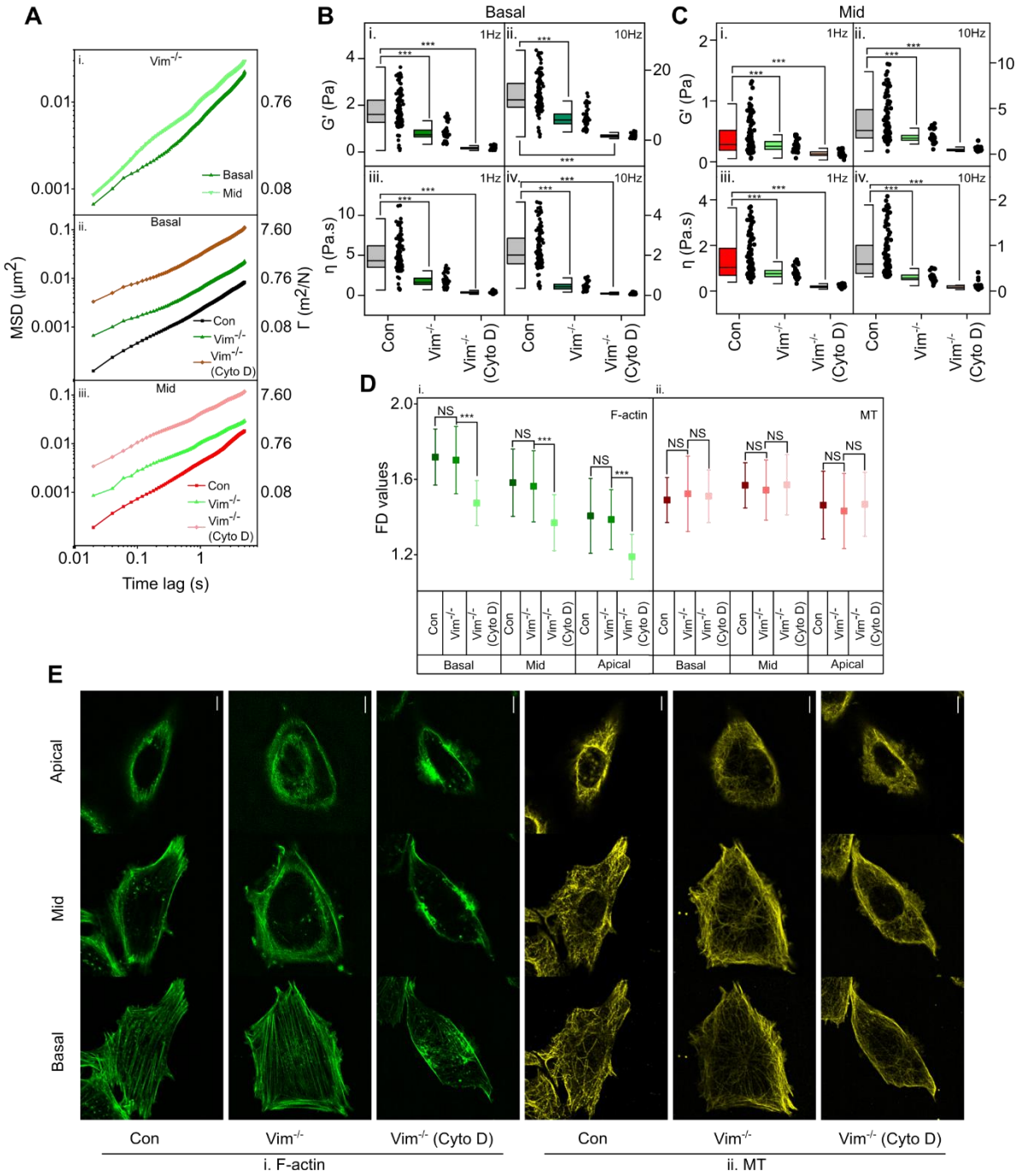

984

985 **Figure 4: Localised vimentin assembly stiffens mid cytoplasm in cytochalasin D**

986 **treated cells.** (**A**) Mean MSD (left axis) and compliance, Γ (right axis) of the basal and

987 mid cytoplasmic regions of Vim$^{-/-}$ cells (i), comparison of Mean MSDs (left axis) and

988 compliance, Γ (right axis) between the control, Vim$^{-/-}$ and Cyto D treated Vim$^{-/-}$ cells

989 across the basal (ii) and mid (iii) cytoplasmic regions. (N_{beads} > 50, N_{cells} > 10) (**B**)
990 Comparison of elastic moduli (G') between the control, $Vim^{-/-}$ and Cyto D treated Vim^{-}
991 $^{/-}$ cells across the basal cytoplasmic region at 1 Hz (i) and 10 Hz (ii) frequencies.
992 Comparison of dynamic viscosity (η) values between the control, $Vim^{-/-}$ and Cyto D
993 treated $Vim^{-/-}$ cells across the basal cytoplasmic region at 1 Hz (iii) and 10 Hz (iv)
994 frequencies. (N_{beads} > 50, N_{cells} > 10; ***p<0.001, Mann-Whitney U test) (**C**)
995 Comparison of elastic moduli (G') between the control, $Vim^{-/-}$ and Cyto D treated Vim^{-}
996 $^{/-}$ cells across the mid cytoplasmic region at 1 Hz (i) and 10 Hz (ii) frequencies.
997 Comparison of dynamic viscosity (η) values between the control, $Vim^{-/-}$ and Cyto D
998 treated $Vim^{-/-}$ cells across the mid cytoplasmic region at 1 Hz (iii) and 10 Hz (iv)
999 frequencies. (N_{beads} > 50, N_{cells} > 10; ***p<0.001, Mann-Whitney U test) (**D**) Fractal
1000 dimension (FD) values of actin and microtubule (MT) filaments in control, $Vim^{-/-}$ and
1001 Cyto D treated $Vim^{-/-}$ cells across the apicobasal axis. (Mean ± SD, N_{cells} > 80;
1002 ***p<0.001, NS, non-significant, two sample T-test) (**E**) Representative confocal
1003 images of F-actin and microtubules (MT) filaments in the control, $Vim^{-/-}$ and Cyto D
1004 treated $Vim^{-/-}$ cells across the apicobasal axis. (Scale bar, 5 μm)

1005

1006 **Figure 5**

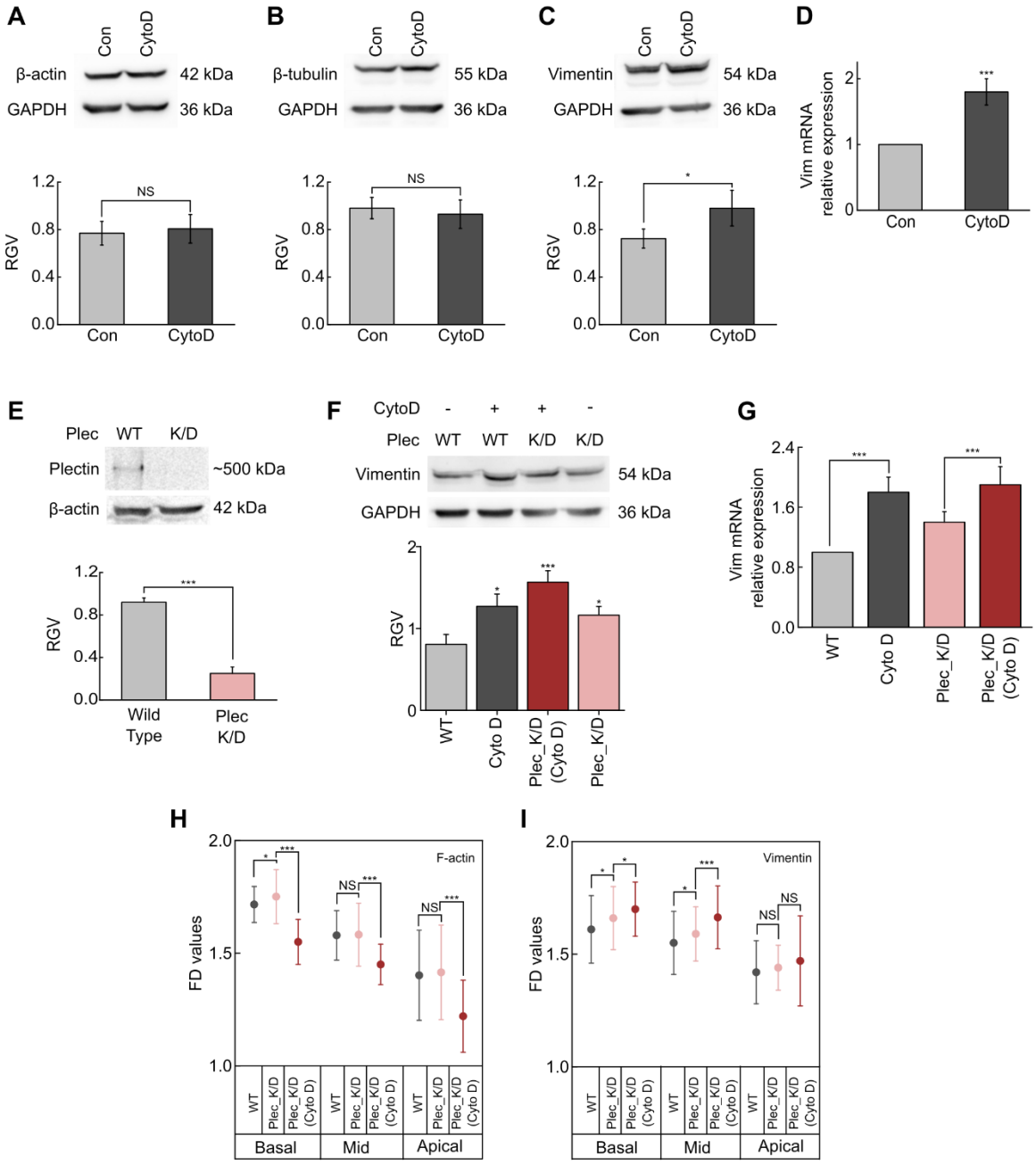

1007

1008 **Figure 5: Plectin directs the localised assembly of vimentin filaments in the mid-**

1009 **cytoplasm of cytochalasin D treated cells.** (**A**) Western blot analysis for β-actin

1010 protein levels post Cyto D (2μM, 1hr) treatment. (n=3, mean ± SD, NS, non-significant,

1011 two sample T test). (**B**) Western blot analysis for β-tubulin protein levels post Cyto D

1012 (2μM, 1hr) treatment. (n=3, mean ± SD, NS, non-significant, two sample T test). (**C**)
1013 Western blot analysis for vimentin protein levels post Cyto D (2μM, 1hr) treatment.
1014 (n=3, mean ± SD, *p<0.05, two sample T test). (**D**) Relative fold change of vimentin
1015 mRNA levels (as quantified by qPCR) post Cyto D treatment (2μM, 1hr). (n=3, mean
1016 ± SD, ***p<0.001, two sample T-test) (**E**) Western blotting analysis of plectin for
1017 confirmation of knockdown. (n=3, mean ± SD, ***p<0.001, two sample T test) (**F**)
1018 Western blot analysis of vimentin expression in wild type and plectin knockdown cells
1019 with and without Cyto D (2μM, 1hr) treatment. (n=3, mean ± SD, *p<0.05, ***p<0.001,
1020 two sample T test) (**G**) Relative fold change of vimentin mRNA levels (as quantified by
1021 qPCR) of wild type and plectin knockdown cells post Cyto D treatment (2μM, 1hr).
1022 (n=3, mean ± SD, *** p <0.001, two sample T-test). Fractal dimension (FD) values of
1023 actin (**H**) and vimentin (**I**) filaments in control, plectin depleted and Cyto D treated
1024 plectin depleted cells across the apicobasal axis. (Mean ± SD, N_{cells} > 80; *p<0.05,
1025 ***p<0.001, NS, non-significant, two sample T-test)

1026

1027 **Figure 6**

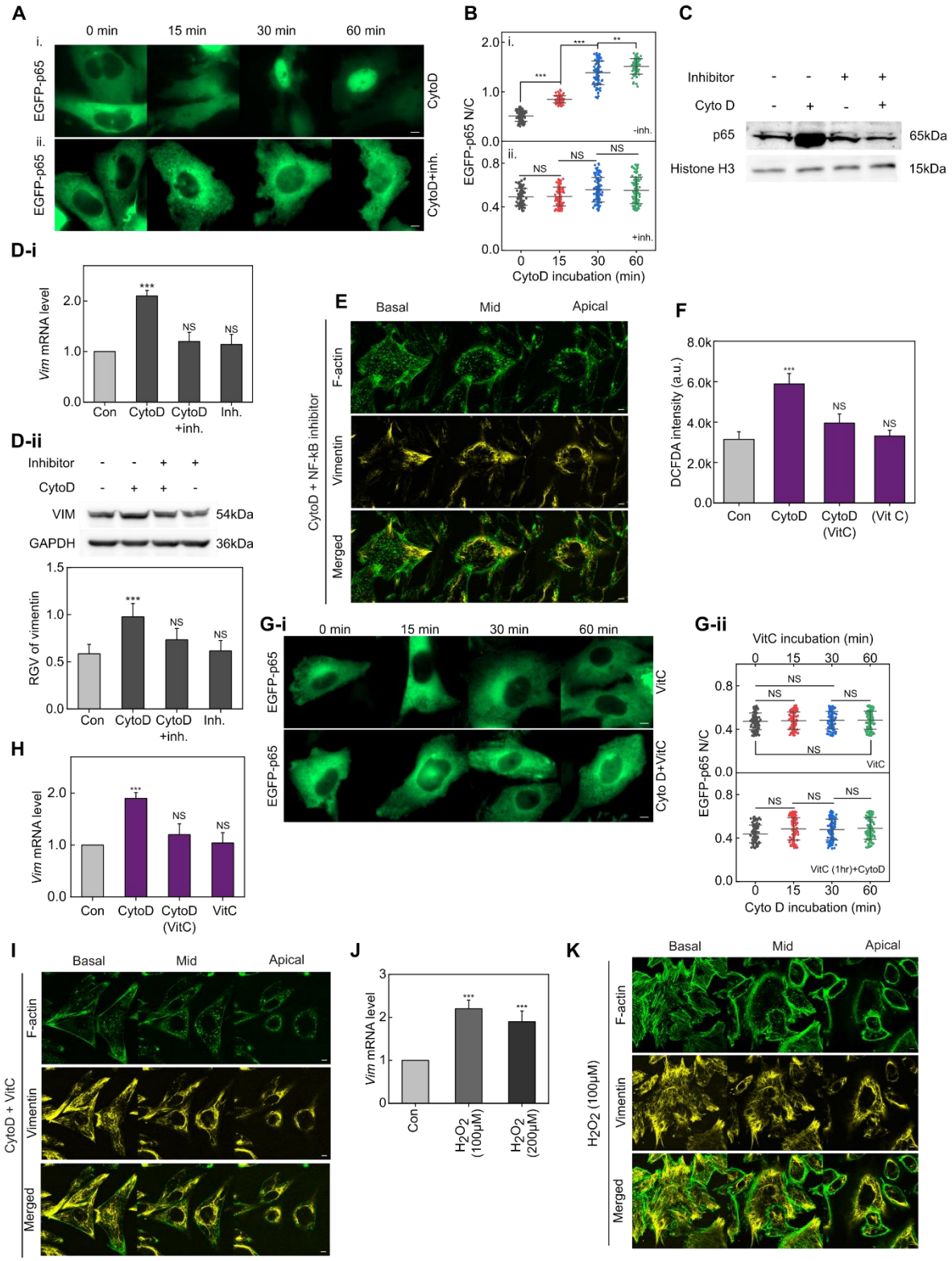

1028

1029 **Figure 6: Cyto D induced assembly of vimentin is dependent on ROS-mediated**

1030 **activation of NF-κB pathway.** (**A**) Representative confocal images of nuclear

1031 translocation of p65-GFP at different time points post Cyto D (2μM) treatment. (Scale
1032 bar, 5μm) (**B**) Nuclear to cytoplasmic (N/C) mean intensity ratio of p65 at different time
1033 points post Cyto D (2μM) treatment with and without NF-κB inhibitor. (N_{Cells} = 80-110
1034 per condition, experimental replicates, n = 3, mean ± SD, **p<0.01, ***p<0.001, NS,
1035 non-significant two sample T test) (**C**) Western blotting analysis of the nuclear fraction
1036 of p65 after Cyto D (2μM, 1hr) treatment in the presence and absence of the NF-κB
1037 inhibitor. (**D-i**) Relative fold changes of vimentin mRNA levels (as quantified by qPCR)
1038 post-Cyto D (2μM, 1hr) treatment with and without NF-κB inhibitor pretreatment. (n =
1039 3, mean ± SD, ***p<0.001, NS, non-significant, two sample T test) (**D-ii**) Western blot
1040 analysis for vimentin protein levels post-Cyto D (2μM, 1hr) treatment with and without
1041 NF-κB inhibitor pretreatment. (n = 3, mean ± SD, ***p<0.001, NS, non-significant, two
1042 sample T test) (**E**) Representative confocal images of F-actin and vimentin at the
1043 basal, mid and apical regions after Cyto D treatment (2μM, 1hr) in the presence of NF-
1044 κB inhibitor. (Scale bar, 5μm) (**F**) Mean DCFDA fluorescence levels of cells after Cyto
1045 D treatment (2μM, 1hr) pre-incubated with vitamin C (Vit C) (n = 3, mean ± SD,
1046 ***p<0.001, NS, non-significant, two sample T test). (**G-i**) Representative images of
1047 nuclear translocation of p65-GFP at different time spans of Vit C incubation (upper
1048 row) and p65-GFP nuclear translocation in cells after Cyto D (2μM) treatment for
1049 various durations following a 1-hour pre-treatment with Vit C (lower row). (Scale bar,
1050 5μm). (**G-ii**) Nuclear to cytoplasmic (N/C) mean intensity ratio of p65 at different Vit C
1051 incubation periods (top) and N/C mean intensity ratio of p65 of cells after Cyto D (2μM)
1052 treatment for various durations following a 1hour pre-treatment with Vit C (bottom).
1053 (N_{cells} = 80-120 per condition, n = 3, mean ± SD, NS, non-significant, two sample T
1054 test). (**H**) Relative fold change of vimentin mRNA levels (as quantified by qPCR) post
1055 Cyto D treatment (2μM, 1hr) with and without Vit C pre-incubation. (n=3, mean ± SD,

1056 ***p<0.001, NS, non-significant, two sample T test). (**I**) Representative confocal
1057 images of F-actin and vimentin at the basal, mid and apical regions after Cyto D
1058 treatment (2μM, 1hr) in the presence of Vit C. (Scale bar, 5μm) (**J**) Relative fold change
1059 of vimentin mRNA levels (as quantified by qPCR) post H_2O_2 incubation (100μM and
1060 200μM). (n=3, mean ± SD, ***p<0.001, two sample T test) (**K**) Representative confocal
1061 images of F-actin and vimentin at the basal, mid and apical regions after H_2O_2
1062 incubation (100μM). (Scale bar, 5μm)

1063

1064 **Supplementary figures with legends**

1065 **Supplementary figure S1**

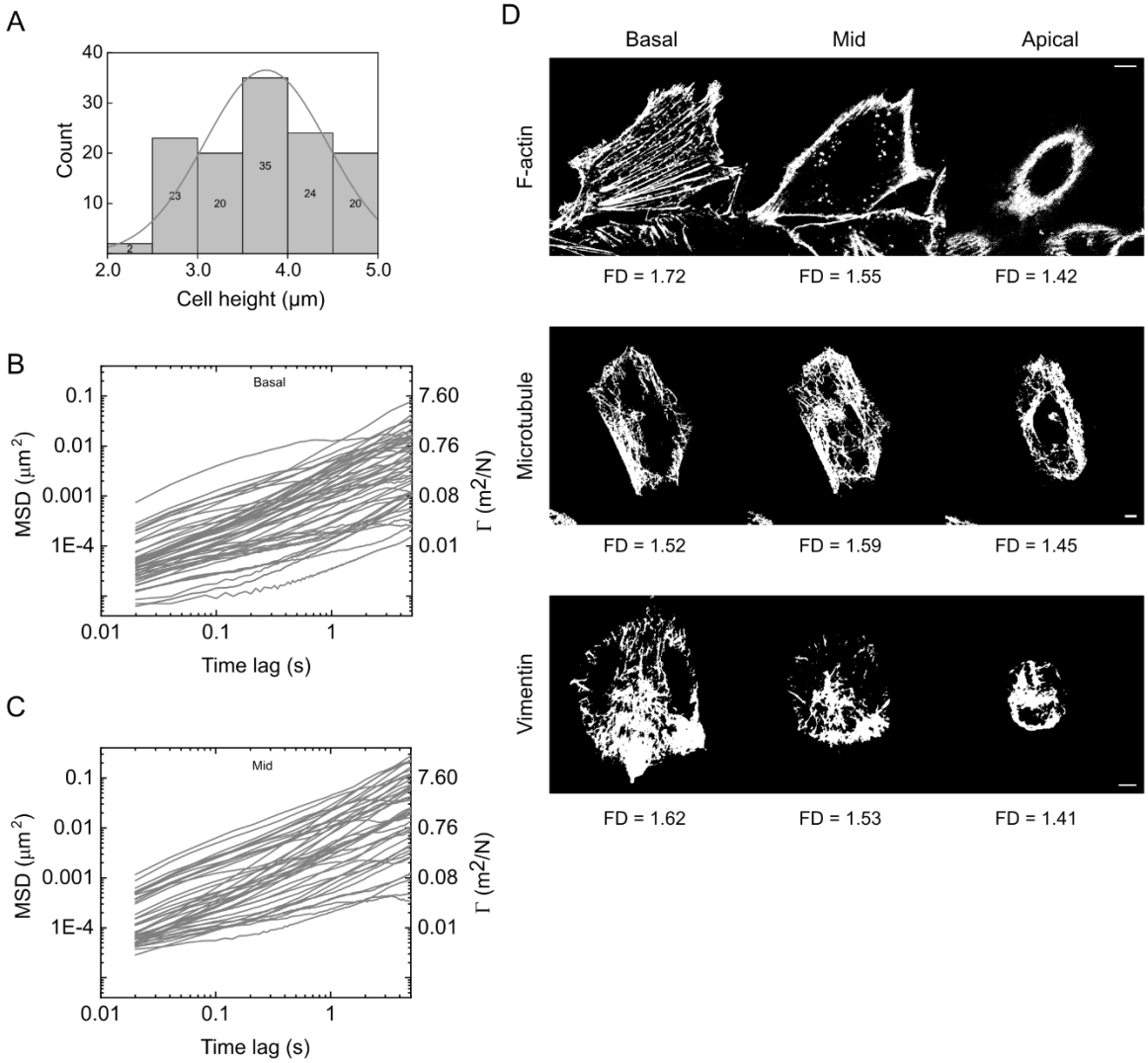

1066

1067 **Figure S1:** (A) Histogram profile of the height of NIH 3T3 cells (N_{cells} > 100). MSDs
1068 (left axis) and compliance, Γ (right axis) values of individual microspheres dispersed
1069 in the basal (B) and mid (C) cytoplasm of control NIH 3T3 cells. (N_{beads} > 60, N_{cells} >
1070 10). (D) Representative binary images of actin, vimentin and microtubule filaments
1071 across the apicobasal axis of control NIH 3T3 cells and their corresponding fractal
1072 dimension (FD) values.

1073 **Supplementary figure S2**

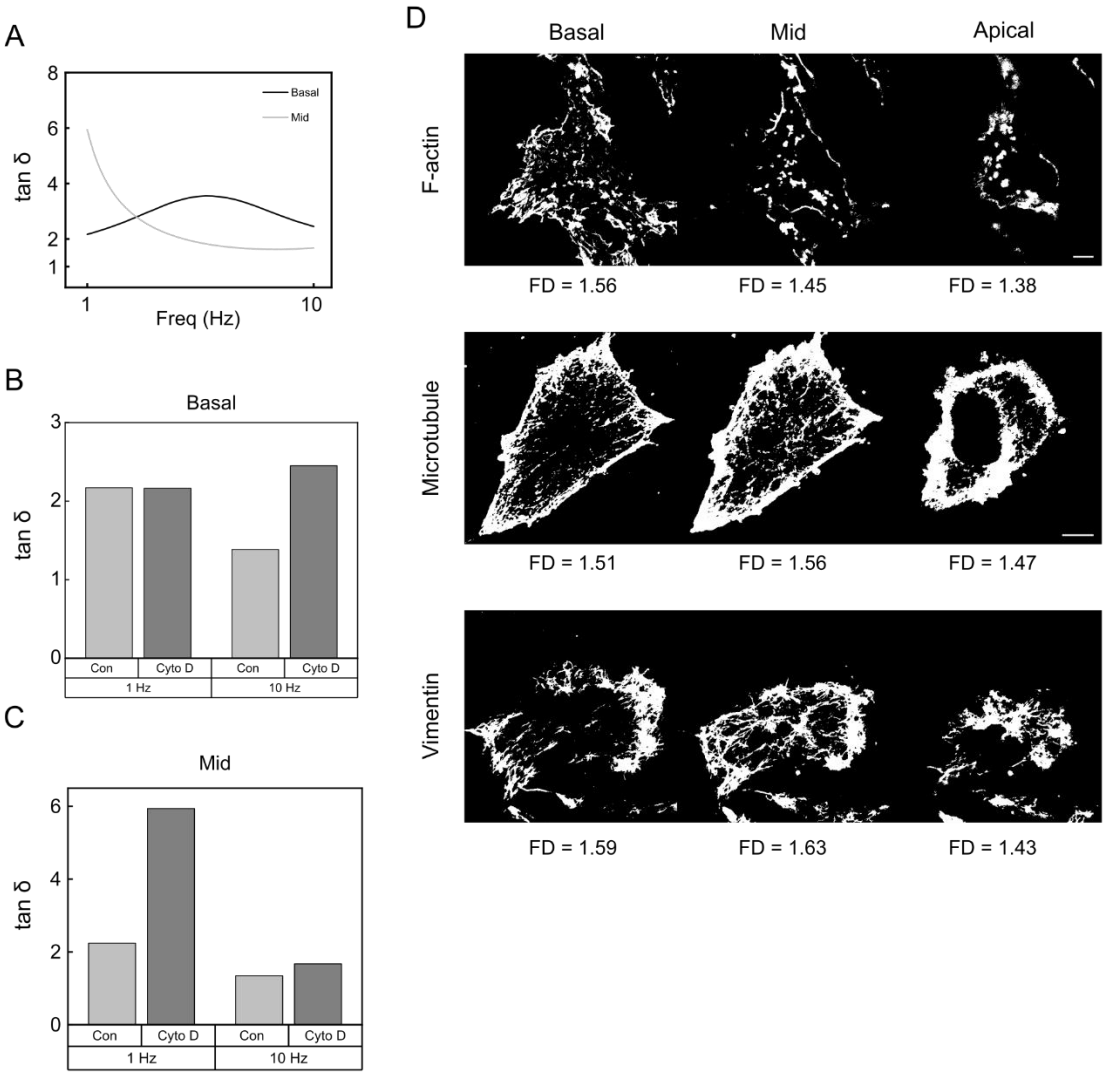

1074

1075 **Figure S2**: (**A**) Mean loss tangent values of the basal and mid cytoplasm of cyto D
1076 treated cells. (**B**) Comparison of tan δ values between control and cyto D treated cells
1077 at the basal cytoplasmic region at 1Hz and 10Hz. (**C**) Comparison of tan δ values
1078 between control and cyto D treated cells at the mid cytoplasmic region at 1Hz and
1079 10Hz frequencies. (**D**) Representative binary images of actin, vimentin and
1080 microtubule filaments across the apicobasal axis of cyto D treated NIH 3T3 cells and
1081 their corresponding fractal dimension (FD) values.

1082 **Supplementary figure S3**

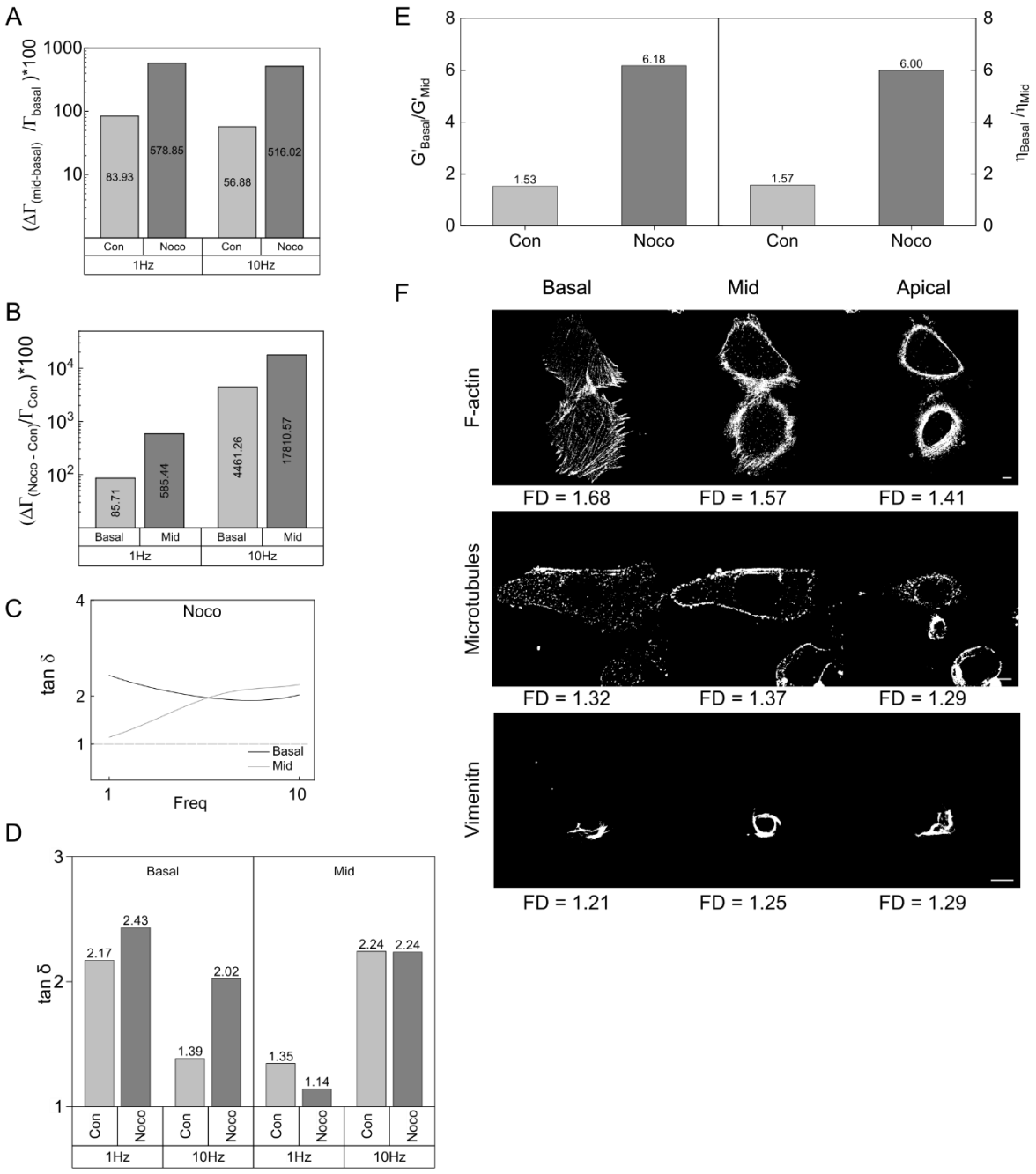

1083

1084 **Figure S3**: (**A**) Relative fold change of the compliance, Γ of the mid cytoplasm
1085 compared to the basal cytoplasm of control and nocodazole treated cells at 1Hz and
1086 10Hz. (**B**) Relative fold change of the compliance, Γ of the nocodazole treated cells
1087 compared to the control cells in the basal and mid cytoplasm at 1Hz and 10Hz. (**C**)

1088 Loss tangent (tan δ) values of the basal and mid cytoplasmic regions of nocodazole
1089 treated cells. (**D**) Comparison of tan δ values between the control and nocodazole
1090 treated cells across the basal and mid cytoplasm at 1Hz and 10Hz. (**E**) Basal to mid
1091 cytoplasmic ratio of elastic modulus (G') and dynamic viscosity (η) in control and
1092 nocodazole treated cells. (**F**) Representative binary images of actin, vimentin and
1093 microtubule filaments across the apicobasal axis of nocodazole treated NIH 3T3 cells
1094 and their corresponding fractal dimension (FD) values.

1095

1096

1097 **Supplementary figure S4**

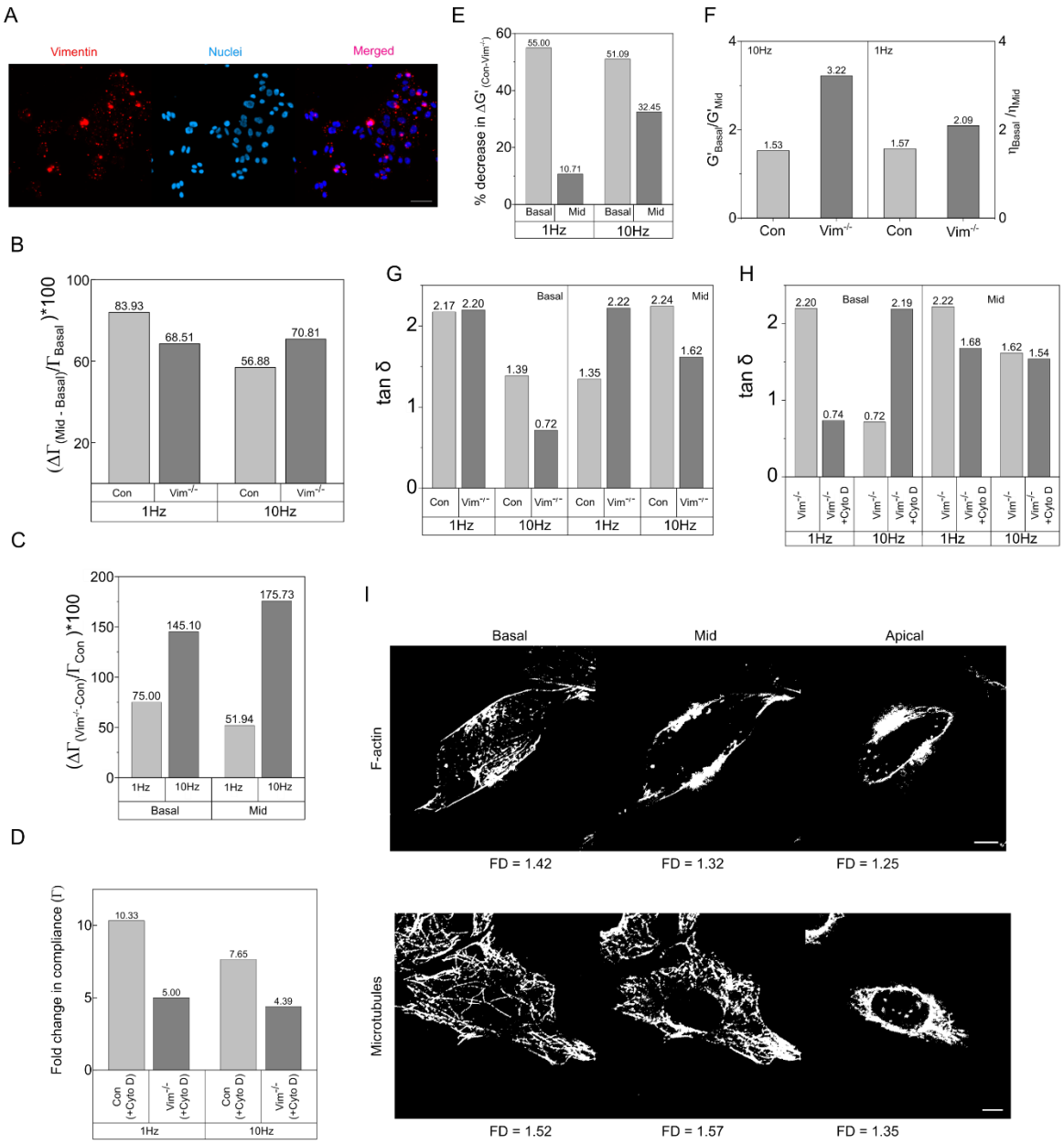

1098

1099 **Figure S4**: (**A**) Representative confocal image validating the knockout of vimentin from
1100 NIH 3T3. (Scale bar, 50μm) (**B**) Relative fold change of the compliance, Γ of the mid
1101 cytoplasm compared to the basal cytoplasm of control and Vim$^{-/-}$ cells at 1Hz and
1102 10Hz. (**C**) Relative fold change of the compliance, Γ of the Vim$^{-/-}$ cells compared to the
1103 control cells in the basal and mid cytoplasm at 1Hz and 10Hz. (**D**) Fold change in the

compliance, Γ of the basal region of control and Vim$^{-/-}$ cells after cyto D treatment at 1Hz and 10Hz. (**E**) Percentage decrease in elastic modulus (G') values upon knockout of vimentin across the basal and mid cytoplasm at 1Hz and 10Hz. (**F**) Basal to mid cytoplasmic ratio of elastic modulus (G') and dynamic viscosity (η) in the control and Vim$^{-/-}$ cells. (**G**) Comparison of tan δ values between the control and Vim$^{-/-}$ cells across the basal and mid cytoplasm at 1Hz and 10Hz. (**H**) Comparison of tan δ values between the Vim$^{-/-}$ and cyto D treated Vim$^{-/-}$ cells across the basal and mid cytoplasm at 1Hz and 10Hz. (**I**) Representative binary images of actin and microtubule filaments across the apicobasal axis of cyto D treated Vim$^{-/-}$ cells and their corresponding fractal dimension (FD) values.

1115 **Supplementary figure S5**

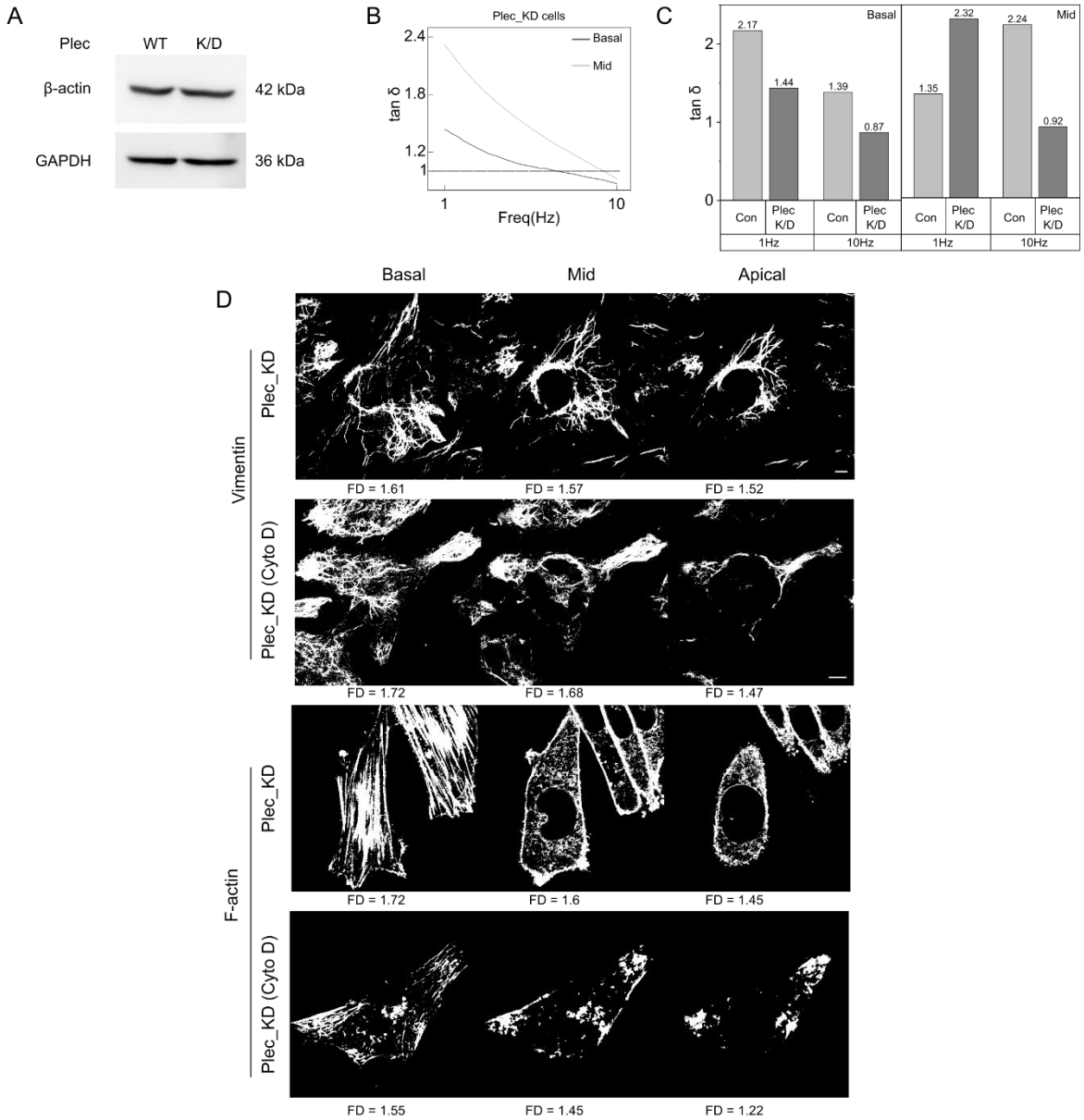

1116

1117 **Figure S5:** (**A**) Western blot analysis of beta-actin in control and plectin depleted NIH
1118 3T3 cells. (**B**) Mean loss tangent values (tan δ) of the basal and mid cytoplasm of
1119 plectin depleted NIH 3T3 cells. (**C**) Comparison of tan δ values between the control
1120 and plectin depleted cells across the basal and mid cytoplasm at 1Hz and 10Hz. (**D**)
1121 Representative binary images of vimentin and actin filaments across the apicobasal

axis of plectin-depleted and cyto D-treated plectin-depleted NIH 3T3 cells, along with their corresponding fractal dimension (FD) values.

1125 **Supplementary figure S6**

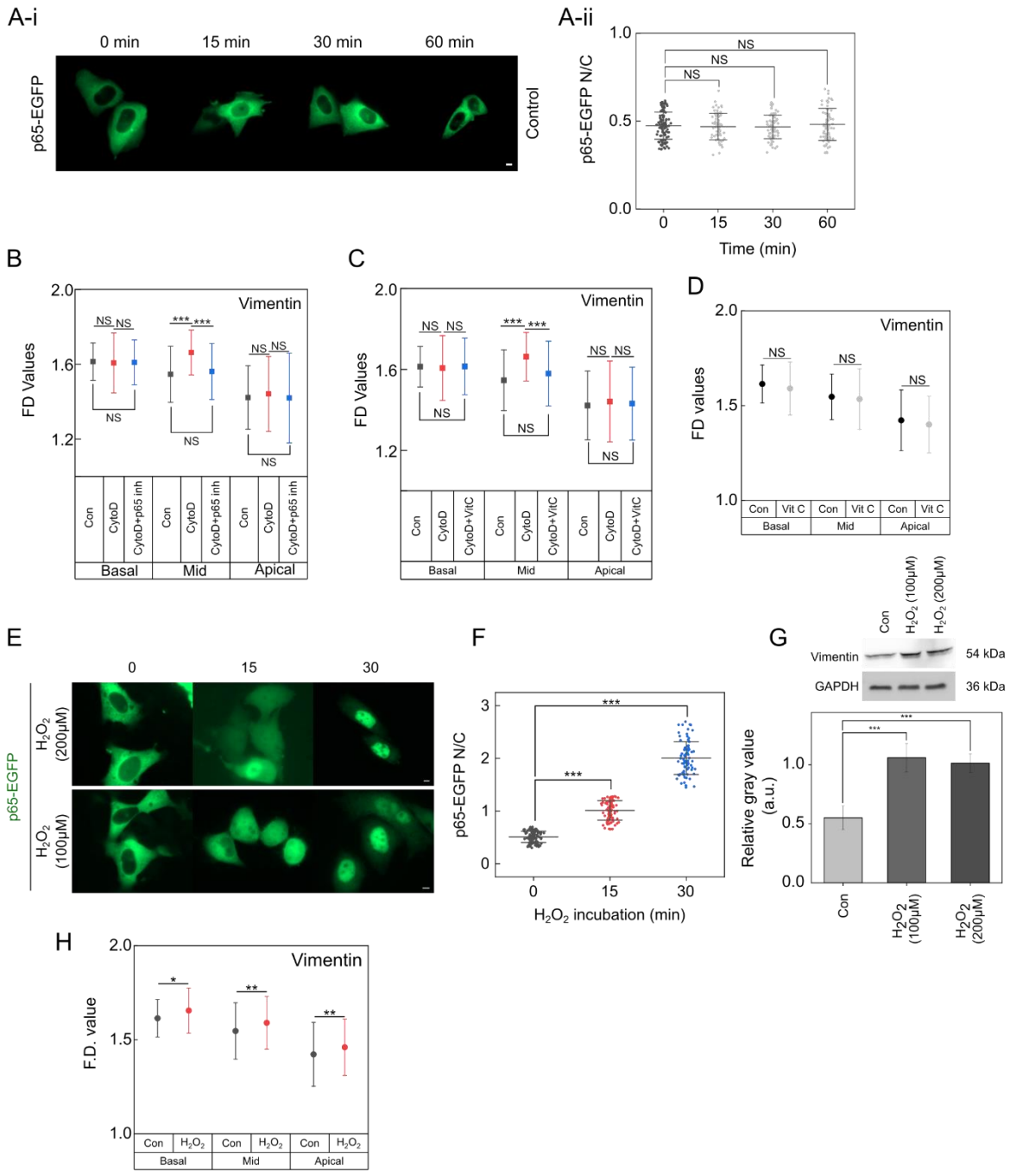

1126

1127 **Figure S6:** (**A**) Tracking of EGFP-p65 localization across different time points (i)
1128 (Scale bar, 5μm) and the corresponding nuclear to cytoplasmic (N/C) mean intensity
1129 ratio values (ii) (Mean ± SD, N_{cells} > 50, NS, non-significant, two sample T test). (**B**)
1130 Quantification of FD values of vimentin in control, cyto D treated and cyto D with p65

1131 inhibitor pretreated cells across the basal, mid and apical cytoplasm. (N_{cells} = 100 -140
1132 per condition, n = 3, mean ± SD, ***p<0.001, NS, non-significant, two sample T test)
1133 (**C**) Quantification of FD values of vimentin in control, cyto D treated and cyto D with
1134 vitamin C pretreated cells across the basal, mid and apical cytoplasm. (N_{cells} > 80, n =
1135 3, mean ± SD, ***p<0.001, NS, non-significant, two sample T test) (**D**) FD values of
1136 control and vitamin C treated cells across the apicobasal axis. (N_{cells} > 100, n = 3,
1137 mean ± SD, NS, non-significant, two sample T test). (**E**) Nuclear translocation of
1138 EGFP-p65 at different time points following H_2O_2 incubation at two different
1139 concentrations. (Scale bar, 5μm) (**F**) Nuclear to cytoplasmic (N/C) mean intensity ratio
1140 of EGFP-p65 at different time points following H_2O_2 incubation. (N_{cells} > 60, ***p<0.001,
1141 two sample T test) (**G**) Western blot analysis of vimentin following H_2O_2 incubation at
1142 two different concentrations. (n = 3, mean ± SD, ***p<0.001, two sample T test) (**H**)
1143 FD analysis of vimentin in control and H_2O_2 treated cells across the apicobasal axis.
1144 (N_{cells} > 80, *p<0.05, **p<0.01, two sample T test)

1145

1146 **Supplementary figure S7**

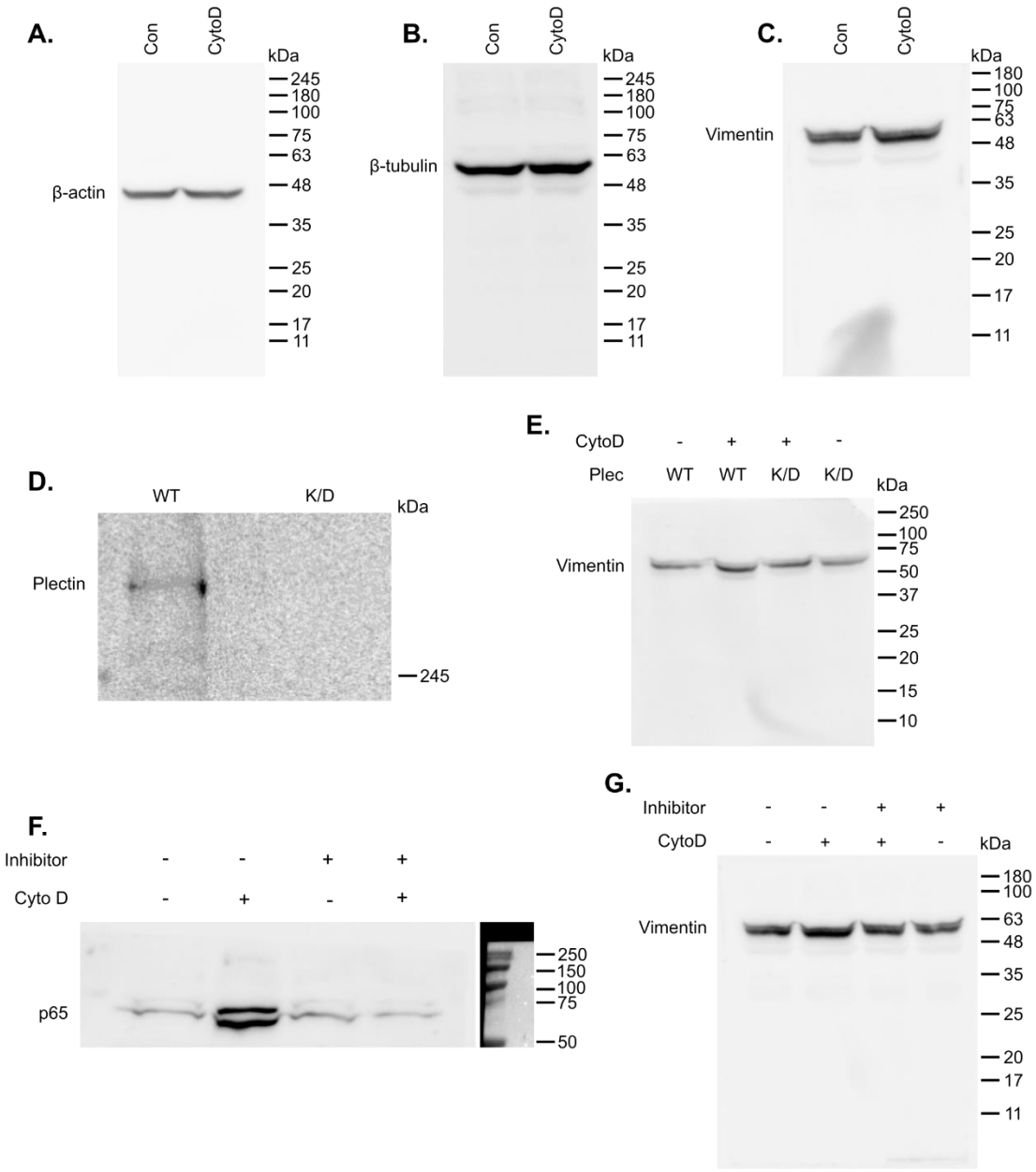

1147

1148 **Figure S7: Blot transparency.** (**A**) Complete western blot of β-actin represented in
1149 Figure 5A. (**B**) Complete western blot of β-tubulin represented in Figure 5B. (**C**)
1150 Complete western blot of vimentin represented in Figure 5C. (**D**) Complete western
1151 blot of plectin represented in Figure 5E. (**E**) Complete western blot of vimentin

1152 represented in Figure 5F. (**F**) Complete western blot of p65 represented in Figure 6C.

1153 (**G**) Complete western blot of vimentin represented in Figure 6D-ii.